This is to certify that the
dissertation entitled

COUPLED ELECTROMAGNETIC THERMAL AND KINETIC
MODELING FOR MICROWAVE PROCESSING OF
POLYMERS WITH TEMPERATURE- AND CURE-
DEPENDENT PERMITTIVITY USING 3D FEM

presented by

RENSHENG SUN

has been accepted towards fulfillment
of the requirements for the

_____Ph.D._____   degree in   _____Electrical Engineering_____

_____
Major Professor's Signature

_____08/22/05_____

Date

PLACE IN RETURN BOX to remove this checkout from your record.
TO AVOID FINES return on or before date due.
MAY BE RECALLED with earlier due date if requested.

DATE DUE	DATE DUE	DATE DUE

2/05 c:/CIRC/DateDue.indd-p.15

COUPLED ELECTROMAGNETIC THERMAL AND KINETIC MODELING FOR
MICROWAVE PROCESSING OF POLYMERS WITH TEMPERATURE- AND
CURE-DEPENDENT PERMITTIVITY USING 3D FEM

By

Rensheng Sun

A DISSERTATION

Submitted to
Michigan State University
in partial fulfillment of the requirements
for the degree of

DOCTOR OF PHILOSOPHY

Department of Electrical and Computer Engineering

2005

ABSTRACT

COUPLED ELECTROMAGNETIC THERMAL AND KINETIC MODELING FOR MICROWAVE PROCESSING OF POLYMERS WITH TEMPERATURE- AND CURE-DEPENDENT PERMITTIVITY USING 3D FEM

By

Rensheng Sun

Polymer processing is an important application of microwave heating in industry. Microwave assisted curing of thermoset polymers has the advantage of heating the polymer precursor materials volumetrically and hence can lead to superior cure with efficiency not available with conventional convection heating. However, due to the complex interactions between the electromagnetic fields and the material, achieving the promise of microwave assisted curing is challenging. This is due to the fact that electrical properties (e.g. the complex permittivity) of the material change non-linearly with temperature and composition during the curing process. Hence, the field distribution within the cavity applicator changes as a function of the extent-of-cure and local temperature of the materials being processed. It is vital in modeling the curing process that the microwave power deposition, heat transfer, and polymer curing kinetics be coupled together.

In this work, we develop a self-consistent 3D marching-in-time multiphysics model, which includes electromagnetic field distribution, microwave power absorption, heat transfer, and polymer curing kinetics. Temperature- and cure-dependent permittivity and curing kinetics for DGEBA/DDS based on experimental data are explicitly included in the model. An edge-based finite element method (FEM) is implemented as an electromagnetic model to ensure the tangential continuity of electric field and

divergence-free condition for source free region, while node-based FEM is used in thermal model to solve for the temperature distribution. The numerical results can be used to determine the time-dependent temperature distribution and curing profile across the polymer sample, as well as the electromagnetic field distribution within the cavity applicator. With the help of this numerical model, robust control strategies can be developed for the polymer curing process. The numerical results are compared with the measured data and a good agreement is achieved.

In this research, the electromagnetic modeling of a novel adaptable multi-feed multimode cylindrical cavity applicator is performed, where the spatial distribution of the electric field can be specified *a priori* to accomplish a desired processing task. The electric field intensity inside the cavity can be tailored by varying the power delivered to each port, and mode-switching can be realized without mechanically adjusting the cavity dimensions. An orthogonal feeding mechanism is developed to reduce the cross coupling between the ports. Numerical simulations are performed for the cavity applicator to verify the theoretical analysis.

To my parents.

ACKNOWLEDGEMENTS

Many people have assisted me on this journey towards the completion of the degree. First of all, I am especially grateful to my advisor Dr. Leo Kempel for his constant encouragement, support, and guidance throughout the years. He has been an outstanding mentor and friend. Appreciation is also given to the other committee members, Dr. Martin Hawley, Dr. Edward Rothwell, and Dr. Andre Benard, for their invaluable guidance during the research. Special thanks are given to Dr. Shanker Balasubramaniam for his insightful suggestions and valuable discussions.

I wish to thank Dr. Liming Zong, Dr. Shuangjie Zhou, Mr. Pedro Barba, and Dr. Gregory Kobidze for their countless help on research topics.

The assistance and friendship of my other fellow graduate students from different departments can not be overstated. I wish to express my sincere thanks to Jun Gao, Chuan Lu, Jun Yuan, Jorge Villa-Giron, Sandra Soto-Caban, Dilip Mandal, Nikki Sgriccia, and Susan Farhat.

I would like to extend my deepest gratitude to my parents, Shouzhi and Jingrong, and my brother, Renhui, for their encouragement and confidence in me during so many years. Finally, but certainly not last, I am especially grateful to my wife Wei for all of her love, support, encouragement, and patience with me throughout my graduate studies.

TABLE OF CONTENTS

LIST OF FIGURES

LIST OF TABLES

CHAPTER 1 INTRODUCTION

Polymer processing is an important application of microwave heating in industry. Microwave assisted curing of thermoset has the advantage of heating the polymer precursor materials volumetrically and hence can lead to superior cure with efficiency not available with conventional convection heating. However, due to the complex interactions between the electromagnetic fields and the material, achieving the promise of microwave assisted curing is challenging. This is due to the fact that electrical properties (e.g. the complex permittivity) of the material change non-linearly with temperature and composition during the curing process. Hence, the field distribution within the cavity applicator changes as a function of the extent-of-cure and local temperature of the materials being processed. It is vital that in modeling the curing process microwave power deposition, heat transfer, and polymer curing kinetics be coupled together.

In this work, first in Chapter 2, the research objectives of this interdisciplinary project are discussed in a little more detail, with the emphasis on the multiphysics modeling and the adaptable multimode applicator design. In Chapter 3, a review of the background on microwave processing of materials is performed, including the electromagnetic fields in a cylindrical single mode cavity and microwave/materials interactions during microwave heating.

In Chapter 4, node-based finite element method (FEM) and edge-based FEM are presented since they will be used for heat transfer model and electromagnetic model separately in the multiphysics model in Chapter 5. Some numerical results generated from EM model are compared with existing data in literature for the purpose of validation of the code.

In Chapter 5, which is the main body of the dissertation, we develop a self-consistent 3D marching-in-time multiphysics model, which includes electromagnetic field distribution, microwave power absorption, heat transfer, and polymer curing kinetics. Temperature- and cure-dependent permittivity and curing kinetics for diglycidyl ether of bisphenol A (DGEBA) / diaminodiphenyl sulfone (DDS) based on experimental data are explicitly included in the model. Edge-based FEM is implemented for electromagnetic model to ensure the tangential continuity of electric field and divergence-free condition for source free region, while node-based FEM is used in thermal model to solve for the temperature distribution. The numerical results can be used to determine the time-dependent temperature distribution and curing profile across the polymer sample, as well as the electromagnetic field distribution within the cavity applicator. With the help of this numerical model, robust control strategies will be developed for the polymer curing process. The numerical results are compared with the measured data and a good agreement is achieved.

In Chapter 6, we present the electromagnetic modeling of a novel adaptable multi-feed multimode cylindrical cavity applicator, where the spatial distribution of the electric field can be specified *a priori* to accomplish a desired processing task. The electric field intensity inside the cavity can be tailored by varying the power delivered to each port, and mode-switching can be realized without mechanically adjusting the cavity dimensions. An orthogonal feeding mechanism is developed to reduce the cross coupling between the ports. Numerical simulations are performed for the cavity applicator to verify the theoretical analysis.

Finally, in Chapter 7 and Chapter 8, we summarize the conclusions and outline the future work, respectively.

CHAPTER 2 RESEARCH OBJECTIVES

2.1 Microwave Heating vs. Conventional Heating

Microwaves are one form of electromagnetic radiation. It is a wave motion associated with electric and magnetic forces. Microwave refers to electromagnetic waves in a frequency range from 300MHz to 300GHz or a free-space wavelength range from 1m to 1mm. Heating is one of the major non-communication applications of microwaves. The fundamental electromagnetic constitutive property of nonmagnetic materials for microwave heating and diagnosis is complex dielectric constant ($\varepsilon^* = \varepsilon' - j\varepsilon''$). The real part of the complex dielectric constant is the dielectric constant, which is related to the microwave energy stored in the materials. The imaginary part is dielectric loss factor, which is related to microwave energy dissipated as heat in materials. The dielectric loss factor of materials is generally due to contributions from the motion of dipoles and charges, conductivity, etc. Polymers have polar groups to interact with electromagnetic fields and exhibit dielectric relaxation. These polar groups can absorb microwave energy directly and the localized heating on the reactive polar sites can initiate or promote polymerizations that require heat.

Microwave processing of materials has been studied as an attractive alternative to conventional thermal processing. Thermal heating is a surface-driven, non-selective process. The heating efficiency is controlled by the heat transfer coefficient at the material surface and the thermal conductivity of the material. During thermal heating, heat flows from the surface to the interior of the material. This tends to cause remarkable temperature gradients in thick materials. Residual thermal stresses resulting from large temperature gradients can impair the physical and mechanical properties of the materials.

In addition, the production cycle is long because of the difficulty in heating poor thermal conductors such as polymers.

Microwave heating offers a number of advantages over thermal heating in a wide range of heating applications. A comparison between microwave and thermal heating is summarized in Table 2.1. Microwave heating is selective, instantaneous, and volumetric with heat loss at the boundaries while thermal heating is nonselective and depends on temperature gradient. Microwave heating can be easily controlled by rapid changes in the applied electric field whereas thermal heating is characterized with long lag times and difficult composite cure control. The heat source of microwave heating can be readily removed to prevent thermal excursion. Microwave processing has potential for rapid processing of thick-section and complex-shaped composites.

Table 2.1 Comparison between microwave and thermal heating methods

Thermal heating	Microwave Heating
Heat conduction/convection	Energy coupling/transport
Surface heating	Molecular level coupling
Slow	Fast
Surface	Volumetric
Non-selective	Selective
Less property dependent	Material property dependent
Surface temperature control	Intelligent control
Established technology	Emerging technology

In recent years, microwave has been investigated as an attractive alternative (and efficient) energy source for material processing, including polymers and composites. Results have been reported on enhanced polymerization rates [1-2], increased glass transition temperatures of cured epoxy [1], improved interfacial bonding between

5

graphite fiber and polymer matrix [3], and increased mechanical properties of the composites [4].

Practical application of microwave heating in industry is however still limited due to difficulties in achieving optimal temperature control for microwave heating. Although microwaves can penetrate materials, thus resulting in volumetric heating, it is not easy to achieve desired field distribution within the material. This is especially true for thermoset polymers. The processing of these polymers involves an autocatalytic reaction (cure) with a large heat of reaction. Curing is difficult to control and uneven cure has detrimental effect on material properties such as mechanical strength. A uniform or controlled temperature history is also desired for reducing residual stress in polymeric composites. This is difficult to achieve without active cooling. It is however possible to initiate cure at precise locations or almost uniformly. In addition to temperature uniformity (or a temperature distribution that minimizes residual stress buildup), curing temperature level is desired to be precisely determined in order to obtain optimal product qualities. For example, a precise temperature cycle should be applied to carbon/epoxy prepregs in order to obtain satisfactory manufactured components in which the matrix crosslinking is almost complete [5].

Hence, the industrial use of microwave as an alternative (energy efficient) approach to inefficient pressurized ovens has been impeded by the lack of proper applicator design, process modeling, and control/monitoring methods. The objective of this interdisciplinary research therefore includes three fundamental elements:

1. Development of a coupled electromagnetic-thermal-kinetic (CETK) multiphysics model that will be used to understand the curing process and to develop

robust control strategies. This combined effects model is unique in that the permittivity (and hence electromagnetic field) variations attributed to temperature and composition changes is explicitly included.

2.   Design of an adaptable multi-feed multimode microwave applicator, where the spatial distribution of the electric field can be specified *a priori* to accomplish a desired task.

3.   Development of a process control methodology that utilizes non-invasive process monitoring.

In this dissertation, the multiphysics process modeling and the adaptable multimode applicator design are emphasized. The process control strategy will be developed later based on the numerical results from the multiphysics model and the new applicator system. Next, the numerical modeling and the applicator design will be discussed in more detail.

2.2 CETK multiphysics modeling

To gain a fundamental understanding of polymer/microwave interactions, to reduce risk, and to help develop control/diagnosis scheme, a multiphysics process simulation package is required. This simulation will include all the relevant physical and chemical properties required to assess the field distribution within the applicator during processing and the resulting temperature profile of the polymer sample. The simulation is supported by three parts: electromagnetic, thermal and curing kinetics modeling.

The critical aspect of our modeling approach relies on the fact that electromagnetic interactions occur much faster, $O(ns)$, than thermal effects, $O(\mu s)$, or the

kinetic/composition effects, $O(s)$. Hence, the electromagnetic analysis can be performed with an efficient steady-state (e.g. time-harmonic) analysis method whose results are used in solving the energy balance equation for heat transfer problem. The numerical results from this process model can be used to determine the time-dependent temperature distribution and curing profile across the polymer sample, as well as the electromagnetic field distribution within the cavity applicator. With the help of this numerical model, robust control strategies can be developed for the polymer curing process.

2.2.1 Electromagnetic Modeling

We are using the edge-based finite element method (FEM) with tetrahedral elements for the applicator and polymer sample since this method offers a high degree of geometrical and electrical fidelity. In particular, the spatial variation in permittivity can readily be accommodated and by using "snapshots-in-time", time-dependant thermal and composition influences on the local permittivity can be included in the model. Recall that such quasi-stationary analysis approaches are valid since the evolution of thermal and composition effects are relatively slow compared to the rate of electromagnetic field oscillation within the applicator.

The finite element method is well-suited for resonant cavity simulation since it can incorporate the presence of a sample as well as determine the response of the system to single frequency excitation in an efficient manner. Once the fields are determined throughout the cavity for a given excitation, local power absorption rate can be determined for the heat transfer model.

2.2.2 Thermal Modeling

Node-based FEM with tetrahedral elements is used for heat transfer model. The temperature distribution will be obtained by solving the energy balance equation, which includes microwave power absorption, heat transfer and heat generation from chemical reactions. After the node-based FEM representing spatial variations is performed, a first-order ordinary differential equation (ODE) system is obtained and the finite difference scheme for temporal variations will be used for time-marching process. The primary heat transfer mechanism within the sample is conduction, while the free convection boundary condition will be applied between the Teflon/air or epoxy/air interfaces.

2.2.3 Curing Kinetics Modeling

As the polymer heats, chemical reactions occur that result in composition changes. Such composition changes lead to different dielectric properties with consequential impact on the electromagnetic fields and power absorption (input power) within the applicator and material. In addition, reaction heat needs to be included in the energy balance equation. For polymer curing, existing reaction kinetics models include an nth-order reaction model [6-7] and an autocatalyzed reaction model [8-10]. The curing reactions for an epoxy are characteristic of autocatalyzed reactions. The reactions between amines and epoxide are autocatalyzed by the hydroxide group formed in the reactions. The generalized form of the autocatalyzed reaction kinetics for epoxy curing was derived from the reaction kinetic mechanism [11]. The extent of reaction can be measured experimentally as a function of time and temperature. The reaction constants and parameters can be determined with regression of experimental data.

9

2.3 Adaptable Applicator Design

Microwave heating is nearly instantaneous, volumetric, and uneven in nature. Heating is most effective when resonant modes are excited inside the microwave applicator, characterized by low power reflectance. Different resonant modes have different electric field distributions, which are typically not uniform. In a multi-mode oven, the applicator is over-moded, time averaged, and heating uniformity can be obtained by frequency sweeping [12]. Single-mode cavities can provide uniform heating using the mode-switching method, in which several modes with complementary heating patterns are alternatively excited [13-14].

With a fixed frequency microwave power source, mode switching can be achieved by mechanically adjusting the volume of the cavity. This mechanical process slows the response of the system to temperature changes. With a variable frequency power source, modes can be changed by changing frequency. As a result of the instantaneous variable frequency mode switching, not only the speed of the process but also the controllability of the process is much improved. Variable frequency mode switched heating of flat graphite/epoxy panels has been presented in a recent paper [15] and dissertation [16]. Results showed the success of controlled uniform heating. However, variable frequency sources are inherently less efficient than the single frequency versions; the equipment is also very expensive. In this research effort, with our novel adaptable multi-feed cavity applicator, mode switching can be obtained by varying the power delivered to multiple ports, hence eliminating the need for mechanical applicator adjustments.

Specifically, this microwave applicator is designed with the goal of:

1. Reducing the processing cycle time.

2. Maximizing the processing efficiency (e.g. maximize power delivered to the material at desired locations and at the desired moment in time).

3. Improving processed material uniformity.

The applicator developed in this effort will be unique since:

1. It is a multi-port, multi-mode applicator that operates at a single frequency using a coherent high-power source.

2. Since the input power is divided between several ports, the applicator can be constructed using components rated for low power application. The use of such components will reduce applicator construction cost.

In this adaptable multimode cavity applicator, we can tailor the field intensity to achieve high field strength in the regions of the applicator requiring high fields (and hence regions where heating is desirable) and low field intensities in regions where heating is not desired. And as we mentioned earlier, this can be done by just varying the power delivered to each port, and the mode-switching can be realized without mechanically adjusting the cavity dimensions. An orthogonal feeding mechanism is developed to reduce the cross coupling between the ports. Numerical simulations are performed for the cavity applicator to verify the theoretical analysis.

CHAPTER 3 BACKGROUND ON MICROWAVE HEATING

3.1 Electromagnetic Fields in a Microwave Enclosure

Electromagnetic field strength and distribution patterns are essential factors that influence microwave heating efficiency and uniformity. They are determined by microwave operating conditions, applicator dimensions, and material properties. To understand microwave heating characteristics, fundamentals of microwave processing are reviewed.

3.1.1 Maxwell's Equations

The basic laws governing electromagnetic wave phenomena are Maxwell's equations, which describe the relations and variations of the electric and magnetic fields, charges, and currents associated with electromagnetic waves. Maxwell's equations can be written in either differential or integral form. The differential form is widely used to solve electromagnetic boundary-value problems and is useful for FEM formulations. These coupled partial differential equations (PDE) are given by

$$\nabla \times \mathbf{E} = -\frac{\partial \mathbf{B}}{\partial t} \text{ (Faraday's law)} \tag{3.1}$$

$$\nabla \times \mathbf{H} = \mathbf{J} + \frac{\partial \mathbf{D}}{\partial t} \text{ (Ampere's law)} \tag{3.2}$$

$$\nabla \cdot \mathbf{D} = \rho \text{ (Gauss law)} \tag{3.3}$$

$$\nabla \cdot \mathbf{B} = 0 \text{ (Gauss law - magnetic)} \tag{3.4}$$

where **E** is the electric field intensity, **H** is the magnetic field intensity, **D** is the electric displacement density or electric flux density, **B** is the magnetic flux density, **J** is the electric current density, and ρ is the charge density. **D** is defined as:

$$\mathbf{D} = \varepsilon_0 \mathbf{E} + \mathbf{P} \tag{3.5}$$

where ε_0 is the dielectric constant of free space, **P** is the volume polarization, the measure of the density of electric dipoles. **B** can be expressed as:

$$\mathbf{B} = \mu_0 (\mathbf{H} + \mathbf{M}) \tag{3.6}$$

where μ_0 is the permeability of free space, **H** is the magnetic field intensity, and **M** is the volume magnetization, the measure of the density of magnetic dipoles in the material. In a simple isotropic medium, these field quantities are related as follows:

$$\mathbf{D} = \varepsilon \mathbf{E} \tag{3.7}$$

$$\mathbf{B} = \mu \mathbf{H} \tag{3.8}$$

where ε is the dielectric constant, and μ is the permeability.

In addition to the Maxwell's Equations, the Equation of Continuity holds due to the conservation of electric charge:

$$\nabla \cdot \mathbf{J} + \frac{\partial}{\partial t}\rho = 0 \tag{3.9}$$

In Maxwell's equations, only two of the PDEs are independent. Usually Equations 3.1 and 3.2 are used with Equation 3.9 to solve for electromagnetic fields.

Maxwell's equations are first-order differential equations with **E** and **B** coupled. They can be converted into decoupled second-order wave equations through mathematical manipulations:

13

$$[\nabla^2 - \mu\sigma\frac{\partial}{\partial t} - \mu\varepsilon\frac{\partial^2}{\partial t^2}]\begin{Bmatrix}\mathbf{E}\\\mathbf{B}\end{Bmatrix} = \begin{Bmatrix}\nabla(\frac{\rho}{\varepsilon}) + \mu\frac{\partial \mathbf{J}^s}{\partial t}\\ \\ -\mu\nabla \times \mathbf{J}^s\end{Bmatrix} \qquad (3.10)$$

where σ is the conductivity, and **J^s** is the source current term. In a source free region, Equations 3.10 becomes:

$$[\nabla^2 - \mu\sigma\frac{\partial}{\partial t} - \mu\varepsilon\frac{\partial^2}{\partial t^2}]\begin{Bmatrix}\mathbf{E}\\\mathbf{B}\end{Bmatrix} = 0 \qquad (3.11)$$

Equations 3.1-3.4 are the time-domain representation of Maxwell's equations. If the source functions, J(r, t) and ρ(r, t), oscillate with a constant angular frequency ω in the system, all the fields will oscillate at the same frequency. The Maxwell's equations can be written in time-harmonic form:

$$\begin{cases}\nabla \times \mathbf{E}(\mathbf{r}) = -j\omega\mathbf{B}(\mathbf{r})\\\nabla \times \mathbf{H}(\mathbf{r}) = \mathbf{J}(\mathbf{r}) + j\omega\mathbf{D}(\mathbf{r})\\\nabla \cdot \mathbf{D}(\mathbf{r}) = \rho(\mathbf{r})\\\nabla \cdot \mathbf{B}(\mathbf{r}) = 0\end{cases} \qquad (3.12)$$

For the time-harmonic case, Equation 3.10 becomes the vector Helmholtz equation and Equation 3.11 becomes the vector Helmholtz equation in source-free region:

$$[\nabla^2 + \omega^2\mu\varepsilon^*]\begin{Bmatrix}\mathbf{E}\\\mathbf{B}\end{Bmatrix} = 0 \qquad (3.13)$$

$$\varepsilon^* = \varepsilon(1 - j\frac{\sigma}{\omega\varepsilon}) \qquad (3.14)$$

where ε* is the complex dielectric constant. Note that isotropic, non-magnetic materials are assumed throughout this thesis.

14

3.1.2 Resonant Modes in a Cylindrical Single Mode Cavity

In a cylindrical single mode cavity, there are two types of resonant modes, transverse electric (TE) and transverse magnetic (TM). In TE modes, the electric field components are transverse, and the magnetic field components are parallel to the direction of wave propagation, which is the axial direction. In TM modes, the electric field components are parallel, and the magnetic field components are transverse to the direction of wave propagation. Three subscripts, n, p, and q, are used to describe the corresponding mode in an empty cavity, i.e. TE_{npq} and TM_{npq}. The subscript n denotes the number of the periodicity in the circumferential direction, n=0,1,2...; p denotes the number of zeroes of the radial wave function, p=1,2,3...; q denotes the number of half wavelengths along the length of the equivalent circular waveguide, q=0,1,2... for TM modes and q=1,2,3... for TE modes.

Theoretically the relationship between the frequency and cavity diameter and length for a given resonant mode can be calculated in closed form. The equations for TE and TM modal resonant frequency for an empty cylindrical single mode cavity [17] are:

$$(f)_{npq}^{TE} = \frac{1}{2\pi a \sqrt{\mu\varepsilon}} \sqrt{x'_{np}{}^2 + \left(\frac{q\pi a}{h}\right)^2} \qquad (3.15)$$

$$(f)_{npq}^{TM} = \frac{1}{2\pi a \sqrt{\mu\varepsilon}} \sqrt{x_{np}{}^2 + \left(\frac{q\pi a}{h}\right)^2} \qquad (3.16)$$

where f is frequency, a is cavity radius, h is cavity height, x_{np} and x'_{np} are the tabulated zeroes of the Bessel's function and the derivative of the Bessel's function, respectively. Fig. 3.1 and Fig. 3.2 show the calculated resonant frequency as a function of cavity length in an empty cavity with a radius of 10.75 cm for TM and TE modes, respectively.
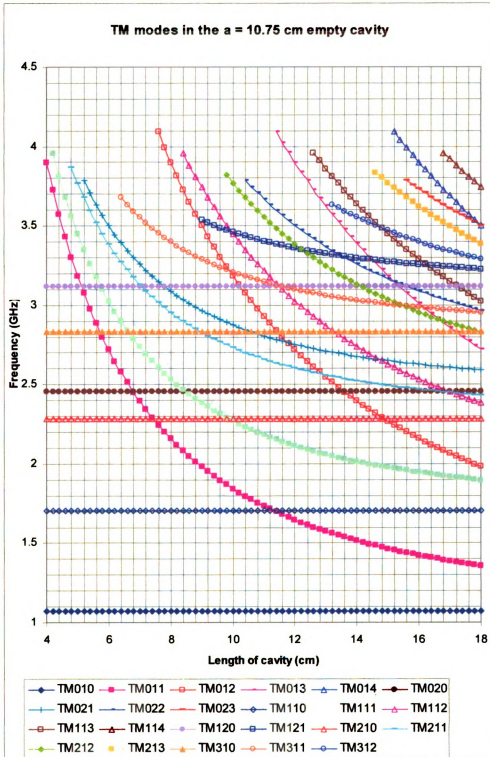
Figure 3.1 TM mode diagram for an empty cavity with a radius of 10.75 cm.
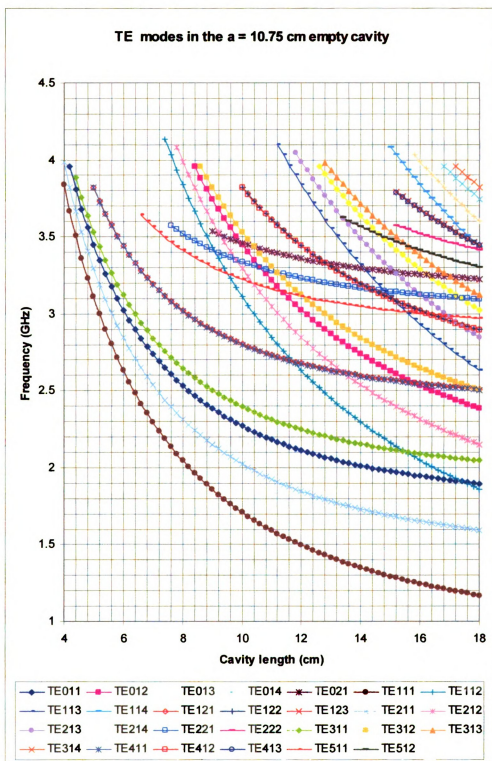
Figure 3.2 TE mode diagram for an empty cavity with a radius of 10.75 cm.

3.1.3 Electromagnetic Fields in a Cylindrical Single Mode Cavity

In a homogeneous, source-free cylindrical single mode cavity with perfectly conducting walls, the electromagnetic fields inside the cavity can be derived from Maxwell's equations and boundary conditions.

For TE modes, the electromagnetic field components inside an empty cavity are [17]:

$$H_\rho = \frac{1}{j\omega\mu}\frac{\partial^2\psi_{npq}}{\partial\rho\partial z} \qquad\qquad E_\rho = -\frac{1}{\rho}\frac{\partial\psi_{npq}}{\partial\phi}$$

$$H_\phi = \frac{1}{j\omega\mu}\frac{1}{\rho}\frac{\partial^2\psi_{npq}}{\partial\phi\partial z} \qquad\qquad E_\phi = \frac{\partial\psi_{npq}}{\partial\rho} \qquad\qquad (3.17)$$

$$H_z = \frac{1}{j\omega\mu}\left(\frac{\partial^2\psi_{npq}}{\partial z^2} + k^2\psi_{npq}\right) \qquad E_z = 0$$

where (ρ, ϕ, z) are the cylindrical coordinates, $k^2 = \omega^2\mu\,\varepsilon$, and ψ_{npq} is the wave potential for TE_{npq} modes:

$$\psi_{npq} = J_n(\frac{x'_{np}}{a}\rho)\begin{Bmatrix}\sin n\phi\\\cos n\phi\end{Bmatrix}\sin(\frac{q\pi}{h}z) \qquad\qquad (3.18)$$

where a is the radius, and h is the height of the cavity.

In TM modes, the field components inside an empty cavity are [17]:

$$E_\rho = \frac{1}{j\omega\varepsilon}\frac{\partial^2\psi_{npq}}{\partial\rho\partial z} \qquad\qquad H_\rho = \frac{1}{\rho}\frac{\partial\psi_{npq}}{\partial\phi}$$

$$E_\phi = \frac{1}{j\omega\varepsilon}\frac{1}{\rho}\frac{\partial^2\psi_{npq}}{\partial\phi\partial z} \qquad\qquad H_\phi = -\frac{\partial\psi_{npq}}{\partial\rho} \qquad\qquad (3.19)$$

$$E_z = \frac{1}{j\omega\varepsilon}(\frac{\partial^2 \psi_{npq}}{\partial z^2} + k^2 \psi_{npq}) \qquad H_z = 0$$

where ψ_{npq} is the wave potential for TM_{npq} modes:

$$\psi_{npq} = J_n(\frac{x_{np}}{a}\rho) \begin{Bmatrix} \sin n\phi \\ \cos n\phi \end{Bmatrix} \cos(\frac{q\pi}{h}z) \qquad (3.20)$$

When the cavity is loaded with materials, equations (3.17)-(3.20) are no longer applicable and numerical techniques can be used to solve for the electromagnetic field inside the cavity. The most widely used numerical techniques include the method of moments (MOM), the finite element method (FEM), and the finite difference time domain (FDTD).

3.2 Microwave/Materials Interactions

3.2.1 Mechanisms of Microwave/Materials Interactions

Non-magnetic materials are classified into conductors, semiconductors and dielectrics according to their electric conductivity. Conductors contain free charges, which are conducted inside the material with alternating electric fields so that a conductive current is induced. Electromagnetic energy is dissipated into the materials while the conduction current is in phase with the electric field inside the materials. Dissipated energy is proportional to conductivity and the square of the electric field strength. Conduction requires long-range transport of charges.

In dielectric materials, electric dipoles are created when an external electric field is applied and they will rotate until they are aligned in the direction of the field.

Therefore, the normal random orientation of the dipoles becomes ordered. These ordered polar segments tend to relax and oscillate with the field. The energy used to hold the dipoles in place is dissipated as heat into the material while the relaxation motion of dipoles is out of phase with the oscillation of the electric field. Both the conduction and the electric dipole movement cause losses and are responsible for heat generation during microwave processing. The contribution of each loss mechanism largely depends on the types of materials and operating frequencies. Generally, conduction loss is dominant at low frequencies while polarization loss is important at high frequencies. Most dielectric materials can generate heat via both loss mechanisms.

There are mainly four different kinds of dielectric polarization:

1. Electron or optical polarization occurs at extremely high frequencies, close to ultraviolet range of electromagnetic spectrum [18, 19]. It refers to the displacement of the electron cloud center of an atom relative to the center of the nucleus, caused by an external electric field. When no electric field is applied, the center of positive charges (nucleus) coincides with the center of negative charges (electron cloud). When an external electric field is present, the electrons are pushed away from their original orbits and electric dipoles are created.

2. Atomic polarization is also referred to as ionic polarization. It occurs in the infrared region of the electromagnetic spectrum. This type of polarization is usually observed in molecules consisting of two different kinds of atoms. When an external electric field is applied, the positive charges move in the direction of the field and the negative ones move in the opposite direction. This

mainly causes the bending and twisting motion of molecules. Atomic polarization can occur in both non-ionic and ionic materials. The magnitudes of atomic polarization in non-ionic materials are much less than that in ionic or partially ionic materials.

3. Orientation or dipole alignment polarization occurs in the microwave range of the electromagnetic spectrum. It is the dominant polarization mechanism in microwave processing of dielectrics. Orientation polarization is usually observed when dipolar or polar molecules are placed in an electric field. At the presence of external electric field, the dipoles will rotate until they are aligned in the direction of the field. The dipolar rotation of molecules is accompanied by intermolecular friction, which is responsible for heat generation. Orientation polarization is fundamentally different from electronic and atomic polarization. The latter is due to the fact that the external field induces dipole moments and exerts displacing force on the electrons and atoms, while the orientation polarization is because of the torque action of the field on the pre-existing permanent dipole moments of the molecules.

4. Interfacial or space charge polarization occurs at low frequencies, e.g. radio frequency (RF). It is a fundamental polarization mode in semiconductors. This type of polarization is caused by the migration of charges inside and at the interface of dielectrics under a large scale field.

3.2.2 Dielectric Properties

Most polymers and composites are non-magnetic materials. The electromagnetic energy loss is only dependent on the electric field. Incident electromagnetic fields can interact with conductive and nonconductive materials. The fundamental electromagnetic property of non-magnetic materials for microwave heating and diagnosis is the complex dielectric constant:

$$\varepsilon = \varepsilon' - j\varepsilon'' \qquad (3.17)$$

The real part of the complex dielectric constant is dielectric constant. The larger the polarizability of a molecule is, the larger its dielectric constant. The imaginary part is dielectric loss factor, which is related to energy dissipated as heat in the materials. Usually, the relative values with respect to the dielectric constant of free space are used:

$$\varepsilon = \varepsilon_0 (\varepsilon_r' - j\varepsilon_{eff}'') \qquad (3.18)$$

where ε_0 is the dielectric constant of free space, ε_r' is the relative dielectric constant, and ε_{eff}'' is the effective relative dielectric loss factor. Typically, the loss factor of materials consists of both polarization and conduction loss. The polarization loss is further contributed by all four polarization mechanisms mentioned earlier. The effective relative loss factor is expressed as [19]:

$$\varepsilon_{eff}''(\omega) = \varepsilon_d''(\omega) + \varepsilon_e''(\omega) + \varepsilon_a'' + \varepsilon_s'' + \frac{\sigma}{\varepsilon_0 \omega} \qquad (3.19)$$

where the subscripts d, e, a, and s refer to dipolar, electronic, atomic and space charge polarization, respectively. The loss factor is a function of material structures, compositions, angular frequency, temperature, pressure, etc.

The ratio of the effective loss factor to the dielectric constant is defined as the loss tangent, which is also commonly used to describe dielectric losses:

$$\tan \delta_{eff} = \frac{\varepsilon''_{eff}}{\varepsilon'_r} \qquad (3.20)$$

When introduced into a microwave field, materials will interact with the oscillating electromagnetic field at the molecular level. Different materials will have different responses to the microwave irradiation. Microwave heating of conductive materials, such as carbon fibers and acid solutions, is mainly due to the interaction of the motion of ions or electrons with the electric field. However, conductors with high conductivity will reflect the incident microwaves at their surface and accordingly can not be effectively heated.

The fields attenuate towards the interior of the material due to skin effect, also. For conducting materials, the conducting electrons are limited in the skin area to some extent, which is called the skin depth, d_s. Defined as the distance into the sample, at which the electric field strength is reduced to $1/e$, the skin depth is given by [17]:

$$d_s = \frac{1}{\left(\frac{1}{2}\omega\mu_o\mu_r\sigma\right)^{1/2}} \qquad (3.21)$$

where ω is the angular frequency of the electromagnetic waves in rad/sec, μ_0 (= $4\pi \times 10^{-7}$ H/m) is the permeability of the free space, μ_r is the relative permeability, and σ is the conductivity of the conductor in mhos/m. For example, graphite has $\sigma = 7 \times 10^4$ mhos/m and $d_s = 38.4$ μm at 2.45 GHz. The skin depth decreases as frequency increases. For a perfect conductor, the electric field is reflected and no electric field is induced inside a

perfect conductor at any frequency. Therefore, no electromagnetic energy will be dissipated even though the conductivity of the perfect conductor is infinite. Since the vast majority of the microwave power delivered to the cavity in this work is dissipated in the polymer part rather than the cavity brass, perfect electric conductor will be assumed.

Microwave heating of nonconductive materials, such as polymers, glass fibers, and Kevlar fibers, is mainly due to the interaction of the motion of dipoles with the alternating electric field. Microwave processing of thermosets is self-adjusting. As the crosslinking occurs, the mobility of dipoles decreases because of the "trapping" or reaction and the dielectric loss factor decreases. Energy absorbed by crosslinking molecules decreases and microwaves are concentrated in unreacted molecules. During microwave processing of thermoplastics, the dielectric loss factor usually increases with temperature and thermal runaway is likely to occur. Thermal runaway can be prevented by decreasing or even turning off power at a temperature close to thermal excursion. Microwave heating selectivity of polymer composites depends on the magnitude of dielectric loss factor of polymers and fibers. When non-conducting fibers, such as glass, are used, microwaves will selectively heat the polymer matrix. When conducting fibers like graphite are used, energy is preferably absorbed by the conductive fibers and heat is locally conducted from the fiber to the matrix. In this case, loss factor is mainly due to the fiber conductivity and can not be used to diagnose the curing process of the low loss matrix materials.

Dielectric measurement of epoxy curing systems has shown that generally both the dielectric constant and dielectric loss factor increase with temperature and decrease with extent of reaction [20]. This dependence on temperature and extent of reaction is

non-linear. During microwave processing, the dielectric properties of materials change as a result of heating and reaction. This affects the electric field strength and power absorption in the materials. The change in electric field and power absorption in turn affects the temperature and extent of reaction inside the materials. Thus, the modeling of microwave heating is a coupled non-linear problem, which involves Maxwell's equations for solving the electric field strength, a heat transfer equation for obtaining the temperature distribution inside the material, and a reaction kinetic equation for calculating extent of reaction.

CHAPTER 4 FINITE ELEMENT METHOD

The finite element method (FEM) is widely used in computational electromagnetics since it is very efficient on modeling full three-dimensional volumes that have complex geometrical details and material inhomogeneities. Since the edge-based FEM for electromagnetics and node-based FEM for heat transfer, respectively, are used herein in Chapter 5, it is necessary to briefly review the basis functions in 2D and 3D cases in this chapter. More information on the general procedure and detailed formulation on FEM can be easily found in some classic textbooks [21, 22]. In this chapter, some numerical results generated from the EM model are compared with existing data in literature for the purpose of validation of the code.

4.1 Basis Functions for Node-based FEM

The finite element method is used for modeling a wide class of problems by breaking up the computational domain into elements of simple shapes. Suitable interpolation polynomials (commonly referred to as shape or basis functions) are used to approximate the unknown function within each element. Once the shape functions are chosen, it is possible to program a computer to solve complicated geometries by specifying the basis functions, geometry, and forcing functions. Node-based shape functions have been used extensively in civil and mechanical engineering applications, for example in heat transfer problems.

In node-based finite elements, the form of the sought function in the element is controlled by the function values at its nodes. The approximate function can then be expressed as a linear combination of basis functions weighted by the nodal coefficients. If

the function values u_i^e at the nodes are taken as nodal variables, then the approximating

function for a two-dimensional element e with p nodes has the form

$$u^e(x,y) = \sum_{i=1}^{p} u_i^e N_i^e(x,y) \qquad (4.1)$$

Since the expression (4.1) must be valid for any nodal variable u_i^e, the basis function

$N_i^e(x,y)$ must be unity at node i and zero for all remaining nodes within the element.

4.1.1 Triangular Elements

First-order triangular elements are popular in 2D case because they can model

arbitrary geometries very easily. The unknown function u within each element is

approximated as

$$u^e(x,y) = a^e + b^e x + c^e y \qquad (4.2)$$

where a^e, b^e, and c^e are constant coefficients to be determined, and e is the element

number. For a linear triangular element, there are three nodes located at the vertices of

the triangle. Assume that the nodes are numbered counterclockwise (to satisfy a right

hand rule) by numbers 1, 2, and 3, with the corresponding values of u denoted by u_1^e, u_2^e,

u_3^e, respectively. Enforcing (4.2) at the three nodes, the following expressions can be

obtained

$$u_1^e = a^e + b^e x_1^e + c^e y_1^e$$

$$u_2^e = a^e + b^e x_2^e + c^e y_2^e$$

$$u_3^e = a^e + b^e x_3^e + c^e y_3^e$$

where x_j^e and y_j^e (j = 1, 2, 3) denote the coordinate values of the jth node in the eth element.

Solving for the constant coefficients a^e, b^e, and c^e in terms of u_j^e and substituting them back into (4.2) yields

$$u^e(x,y) = \sum_{j=1}^{3} N_j^e(x,y) u_j^e \qquad (4.3)$$

where $N_j^e(x,y)$ are the interpolation or basis functions given by

$$N_j^e(x,y) = \frac{1}{2\Delta^e}(a_j^e + b_j^e x + c_j^e y) \quad j = 1, 2, 3 \qquad (4.4)$$

in which

$$a_1^e = x_2^e y_3^e - y_2^e x_3^e; \quad b_1^e = y_2^e - y_3^e; \qquad c_1^e = x_3^e - x_2^e$$

$$a_2^e = x_3^e y_1^e - y_3^e x_1^e; \quad b_2^e = y_3^e - y_1^e; \qquad c_2^e = x_1^e - x_3^e$$

$$a_3^e = x_1^e y_2^e - y_1^e x_2^e; \quad b_3^e = y_1^e - y_2^e; \qquad c_3^e = x_2^e - x_1^e$$

and

$$\Delta^e = \frac{1}{2} \begin{vmatrix} 1 & x_1^e & y_1^e \\ 1 & x_2^e & y_2^e \\ 1 & x_3^e & y_3^e \end{vmatrix} = \frac{1}{2}(b_1^e c_2^e - b_2^e c_1^e) = \text{area of the } e^{th} \text{ element.}$$

It can be easily shown that these basis functions have the property

$$N_i^e(x_j^e, y_j^e) = \delta_{ij} = \begin{cases} 1 & i = j. \\ 0 & i \neq j. \end{cases} \qquad (4.5)$$

As a result, u^e in (4.3) reduces to its nodal value u_i^e at node i. Another important feature

of $N_j^e(x, y)$ is that it vanishes when the observation point (x,y) is on the element side

opposite the jth node. Therefore, the value of u^e at an element side is not related to the

value of u at the opposite node, but rather, it is determined by the values at the two

endpoints of its associated side. This important feature guarantees continuity of the

solution across the element sides.

A very useful integration formula in terms of the area coordinates — N_1, N_2, N_3

— over a triangular domain is given by [23]

$$\iint_{\Delta^e} \left(N_1^e\right)^l \left(N_2^e\right)^m \left(N_3^e\right)^n dx dy = \frac{l!\,m!\,n!}{(l+m+n+2)!} 2\Delta^e \tag{4.6}$$

4.1.2 Tetrahedral Elements

The three-dimensional analogue of a two-dimensional triangle is a tetrahedron

(four-faced element). Once again, special coordinates, called volume coordinates or

simplex coordinates, can be used to simplify the derivation of shape functions. Let us

consider the tetrahedral element illustrated in Fig. 4.1. Within the element, the unknown

function u can be approximated as (for first-order elements)

$$u^e(x, y, z) = a^e + b^e x + c^e y + d^e z \tag{4.7}$$
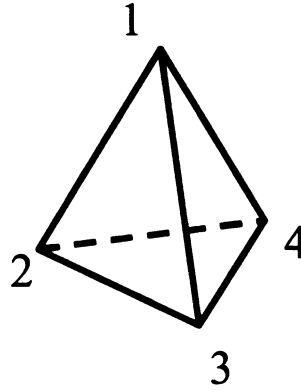
Figure 4.1 Linear tetrahedral element.

The coefficients a^e, b^e, c^e, and d^e can be determined by enforcing (4.7) at the four nodes of the element assuming a given value at the vertices. Thus, denoting the value of u at the jth node as u_j^e, the following expressions can be obtained

$$u_1^e = a^e + b^e x_1^e + c^e y_1^e + d^e z_1^e$$

$$u_2^e = a^e + b^e x_2^e + c^e y_2^e + d^e z_2^e$$

$$u_3^e = a^e + b^e x_3^e + c^e y_3^e + d^e z_3^e$$

$$u_4^e = a^e + b^e x_4^e + c^e y_4^e + d^e z_4^e$$

from which we obtain

$$a^e = \frac{1}{6V^e} \begin{vmatrix} u_1^e & u_2^e & u_3^e & u_4^e \\ x_1^e & x_2^e & x_3^e & x_4^e \\ y_1^e & y_2^e & y_3^e & y_4^e \\ z_1^e & z_2^e & z_3^e & z_4^e \end{vmatrix} = \frac{1}{6V^e}(a_1^e u_1^e + a_2^e u_2^e + a_3^e u_3^e + a_4^e u_4^e)$$

$$b^e = \frac{1}{6V^e} \begin{vmatrix} 1 & 1 & 1 & 1 \\ u_1^e & u_2^e & u_3^e & u_4^e \\ y_1^e & y_2^e & y_3^e & y_4^e \\ z_1^e & z_2^e & z_3^e & z_4^e \end{vmatrix} = \frac{1}{6V^e}(b_1^e u_1^e + b_2^e u_2^e + b_3^e u_3^e + b_4^e u_4^e)$$

$$c^e = \frac{1}{6V^e} \begin{vmatrix} 1 & 1 & 1 & 1 \\ x_1^e & x_2^e & x_3^e & x_4^e \\ u_1^e & u_2^e & u_3^e & u_4^e \\ z_1^e & z_2^e & z_3^e & z_4^e \end{vmatrix} = \frac{1}{6V^e}(c_1^e u_1^e + c_2^e u_2^e + c_3^e u_3^e + c_4^e u_4^e)$$

$$d^e = \frac{1}{6V^e} \begin{vmatrix} 1 & 1 & 1 & 1 \\ x_1^e & x_2^e & x_3^e & x_4^e \\ y_1^e & y_2^e & y_3^e & y_4^e \\ u_1^e & u_2^e & u_3^e & u_4^e \end{vmatrix} = \frac{1}{6V^e}(d_1^e u_1^e + d_2^e u_2^e + d_3^e u_3^e + d_4^e u_4^e)$$

where

$$V^e = \frac{1}{6} \begin{vmatrix} 1 & 1 & 1 & 1 \\ x_1^e & x_2^e & x_3^e & x_4^e \\ y_1^e & y_2^e & y_3^e & y_4^e \\ z_1^e & z_2^e & z_3^e & z_4^e \end{vmatrix} = \text{volume of the element.}$$

The coefficients a_j^e, b_j^e, c_j^e, and d_j^e can be determined from expansion of the determinants.

Substituting the expressions for a^e, b^e, c^e, and d^e back into (4.7), (4.7) becomes

$$u^e(x,y,z) = \sum_{j=1}^{4} N_j^e(x,y,z)u_j^e \tag{4.8}$$

where the interpolation functions $N_j^e(x,y,z)$ are given by

$$N_j^e(x, y, z) = \frac{1}{6V^e}(a_j^e + b_j^e x + c_j^e y + d_j^e z). \tag{4.9}$$

Similar to the two-dimensional case, it can be shown that the interpolation functions have the property

$$N_i^e(x_j, y_j, z_j) = \delta_{ij} = \begin{cases} 1 & i = j. \\ 0 & i \neq j. \end{cases} \tag{4.10}$$

and furthermore that $N_j^e(x, y, z)$ vanishes when the observation point is on the surface of the tetrahedron opposite the jth node. As a result, facial inter-element continuity of the interpolated function is guaranteed.

Similarly to triangular elements, volume coordinates greatly simplify integration over tetrahedral elements. A useful formula for integrating over the volume of a tetrahedron is [23]

$$\iiint_{V^e} \left(N_1^e\right)^k \left(N_2^e\right)^l \left(N_3^e\right)^m \left(N_4^e\right)^n dV = \frac{k!\,l!\,m!\,n!}{(k + l + m + n + 3)!} 6V^e \tag{4.11}$$

4.2 Basis Functions for Edge-based FEM

In electromagnetics, serious problems are encountered when node-based elements are employed to represent vector electric or magnetic fields. First, spurious modes are observed when modeling cavity problems using node-based elements [24], which is generally attributed to lack of enforcement of the divergence condition. Second, it is inconvenient to impose boundary conditions at material interfaces as well as at conducting surfaces. Third, it is difficult to represent conducting and dielectric edges and corners due to field singularities associated with these structures [25].

Edge-based finite elements, whose degrees of freedom are associated with the edges and the faces of the finite element mesh, have been shown to be free of the above shortcomings. Edge basis functions were described by Whitney [26] over 35 years ago and have been revived by Bossavit and Verite [27], Nedelec [28], and Hano [29] in the recent past. It was Nedelec's landmark paper [28] that laid down the guidelines for constructing finite element basis functions that span a curl conforming space with degrees of freedom associated with the edges, faces, and elements of a finite element mesh.

4.2.1 Triangular Elements

Since the edges of an arbitrary triangular element are not parallel to the x- or y-axis, it is not easy to guess the form of the edge-based basis function by inspection. Therefore, the edge-based basis for a triangular element will be expressed in terms of its area coordinates, L_1^e, L_2^e, L_3^e. These are the Whitney elements. If the local edge numbers are defined according to Table 4.1, then edge bases for a triangular element are defined as

$$\mathbf{W}_i^e = \mathbf{W}_{ij}^e = l_{ij}^e (L_i^e \nabla L_j^e - L_j^e \nabla L_i^e), \qquad i,j = 1, 2, 3 \qquad (4.12)$$

where $\mathbf{W}_i^e$ denotes the basis function for the ith edge of the eth element and l_{ij} is the length of the edge formed by nodes i and j. The vector field inside the triangular element can, therefore, be expanded as

$$\mathbf{E}^e = \sum_{i=1}^{3} E_i^e \mathbf{W}_i^e \qquad (4.13)$$

where E_i^e denotes the tangential field along the ith edge. It can be easily shown that the edge-based functions defined in (4.12) have the following properties within the element

$$\nabla \cdot \mathbf{W}_{ij}^e = 0$$

$$\nabla \times \mathbf{W}_{ij}^e = 2l_{ij}^e \nabla L_i^e \times \nabla L_j^e$$

If $\hat{\mathbf{e}}_1$ is the unit vector pointing from node 1 to node 2, then $\hat{\mathbf{e}}_1 \cdot \nabla L_1 = -1/l_1$ and

$\hat{\mathbf{e}}_1 \cdot \nabla L_2 = 1/l_1$. Since L_1 is a linear function that varies from unity at node 1 and zero at

node2 and L_2 is unity at node 2 and zero at node 1, it is clear that

$$\hat{\mathbf{e}}_1 \cdot \mathbf{W}_{12}^e = L_1^e + L_2^e = 1$$

along the entire length of edge 1. This implies that $\mathbf{W}_{12}^e$ has a constant tangential

component along edge 1. Moreover, since L_1^e vanishes along edge 2, ∇L_1^e is normal to

edge 2, L_2^e vanishes along edge 3, and ∇L_2^e is normal to edge 3, $\mathbf{W}_{12}^e$ has no tangential

component along these edges. Similar observations apply to $\mathbf{W}_{23}^e$ and $\mathbf{W}_{31}^e$. Thus,

tangential continuity is preserved across inter-element boundaries but normal continuity

is not maintained. These are the conditions necessary for vector EM problems.

Table 4.1 Edge numbering for a triangular element

Edge No.	Node i_1	Node i_2
1	1	2
2	2	3
3	3	1

4.2.2 Tetrahedral Elements

Tetrahedra are, by far, the most popular element shapes to be employed for three-

dimensional applications. This is because the tetrahedral element is the simplest

tessellation shape capable of modeling arbitrary three-dimensional geometries and is also well suited for automatic mesh generation. The derivation of shape functions for these elements follow the same pattern as that for triangular vector basis functions. Consider the tetrahedron shown in Fig. 4.1 and define the edge numbers according to Table 4.2, it is clear that

$$\mathbf{W}_i^e = \mathbf{W}_{ij}^e = l_{ij}^e (L_i^e \nabla L_j^e - L_j^e \nabla L_i^e), \qquad i,j = 1, 2, 3, 4 \qquad (4.14)$$

where L_1^e, L_2^e, L_3^e, L_4^e are the basis functions for the node-based tetrahedral elements. The vector field within the element can then be expanded as

$$\mathbf{E}^e = \sum_{i=1}^{6} E_i^e \mathbf{W}_i^e \qquad (4.15)$$

where the coefficients E_i^e represent the average value of the field along the ith edge of the eth element.

Table 4.2 Edge definition for a tetrahedral element

Edge No.	Node i_1	Node i_2
1	1	2
2	1	3
3	1	4
4	2	3
5	4	2
6	3	4

An elegant explanation of the physical character of the edge-based interpolation function is given by Bossavit [30]. Let us consider edge number 1 connecting nodes 1 and 2 in Fig. 4.1. Since ∇L_2^e is orthogonal to facet {134} and ∇L_1^e is orthogonal to facet

{234}, the field turns around the axis 3-4 and is normal to planes containing nodes 3 and 4. The field thus has only tangential continuity across element faces. Edge elements can also be described as Whitney elements of degree one and can be broadly classified as belonging to the H^0(curl) space.

When the edge-based basis functions are employed for a three-dimensional finite element discretization of a vector wave equation, after applying Galerkin testing and the vector identity, the resulting elemental matrices contain the following two integrals [22]:

$$E_{ij}^e = \iiint_{V^e} (\nabla \times \mathbf{W}_i^e) \cdot (\nabla \times \mathbf{W}_j^e) dV \qquad (4.16)$$

$$F_{ij}^e = \iiint_{V^e} \mathbf{W}_i^e \cdot \mathbf{W}_j^e dV. \qquad (4.17)$$

These two integrals can be evaluated analytically for tetrahedral element. If we adopt the expression given in (4.14), the curl of $\mathbf{W}_i^e$ is given by

$$\nabla \times \mathbf{W}_i^e = 2l_i^e \nabla L_{i_1}^e \times \nabla L_{i_2}^e$$

$$= \frac{2l_i^e}{(6V^e)^2} \left[\left(c_{i_1}^e d_{i_2}^e - d_{i_1}^e c_{i_2}^e \right) \hat{x} + \left(d_{i_1}^e b_{i_2}^e - b_{i_1}^e d_{i_2}^e \right) \hat{y} + \left(b_{i_1}^e c_{i_2}^e - c_{i_1}^e b_{i_2}^e \right) \hat{z} \right]$$

$$(4.18)$$

where b_i^e, c_i^e, and d_i^e are defined in Section 4.1.2. Substituting (4.18) into (4.16), (4.16) becomes

$$E_{ij}^e = \frac{4l_i^e l_j^e V^e}{(6V^e)^4} \left[\left(c_{i_1}^e d_{i_2}^e - d_{i_1}^e c_{i_2}^e \right) \left(c_{j_1}^e d_{j_2}^e - d_{j_1}^e c_{j_2}^e \right) \right.$$

$$\left. + \left(d_{i_1}^e b_{i_2}^e - b_{i_1}^e d_{i_2}^e \right) \left(d_{j_1}^e b_{j_2}^e - b_{j_1}^e d_{j_2}^e \right) + \left(b_{i_1}^e c_{i_2}^e - c_{i_1}^e b_{i_2}^e \right) \left(b_{j_1}^e c_{j_2}^e - c_{j_1}^e b_{j_2}^e \right) \right]$$

$$(4.19)$$

For the integral in (4.17), using the expression in (4.14), the dot product is given by

$$\mathbf{W}_i^e \cdot \mathbf{W}_j^e = \frac{l_i^e l_j^e}{(6V^e)^2} \left[L_{i_1}^e L_{j_1}^e f_{i_2 j_2} - L_{i_1}^e L_{j_2}^e f_{i_2 j_1} - L_{i_2}^e L_{j_1}^e f_{i_1 j_2} + L_{i_2}^e L_{j_2}^e f_{i_1 j_1} \right]$$

(4.20)

where $j_{ij} = b_i^e b_j^e + c_i^e c_j^e + d_i^e d_j^e$. Substituting this into (4.17) and utilizing the general

integration formula given in (4.11), each entry in the elemental matrix can be obtained

analytically, as shown in Appendix for completeness.

4.3 Code Validation with Waveguide Applications

In chapter 5, the multiphysics model for polymer processing will be studied,

where the heat transfer model is implemented with node-based elements while the

electromagnetic model is implemented with edge-based elements. Before hand, the EM

code is validated for a couple waveguide applications in this section. These problems

have solution data in literature and are sufficiently general as to validate the code for this

thesis. Regarding the mode-matching boundary condition on the two ports of the

waveguide, the formulations in [22] are used and the details are cited below for

completeness of the section.

The geometry of the problem is illustrated in Fig. 4.2, whose specific

configuration consists of a dielectric and/or metallic obstacle placed in a rectangular

waveguide. As usual, analysis of this problem amounts to solving Maxwell's equations in

the region of interest, which for this problem is the region bounded by the waveguide

walls. Since the waveguide under consideration is assumed to be infinitely long, the

region of interest extends to infinity. To apply the finite element method to such an

unbounded region, it is first necessary to truncate the infinite region to a finite region. This can be accomplished by placing fictitious planes on each of the two sides of the obstacles. These two fictitious planes are denoted by S_1 and S_2, respectively, in Fig. 4.2.
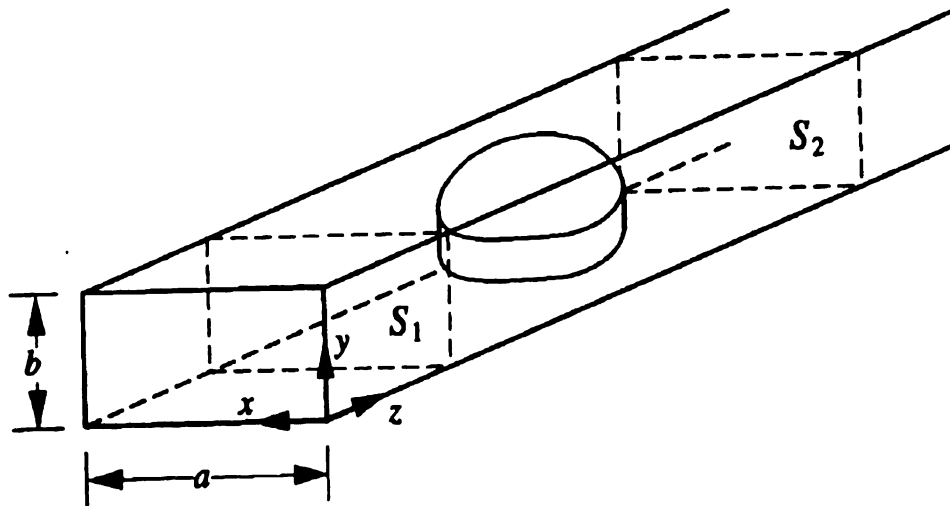

Figure 4.2 Rectangular waveguide loaded with an obstacle [22].

To define the boundary-value problem uniquely for the region bounded by S_1, S_2 and the waveguide walls, it is necessary to prescribe a boundary condition for each of S_1 and S_2. For this, let us assume that the waveguide is operating at a frequency at which only the dominant mode, TE_{10}, can propagate without attenuation. This is a practical assumption. Further, let us assume that S_1 and S_2 are placed sufficiently far from the obstacle so that higher-order modes excited by the obstacle die out before they reach S_1

and S_2. Thus, at S_1 the total field can be expressed as a superposition of an incident TE_{10} wave and a reflected TE_{10} wave. That is,

$$\mathbf{E}(x,y,z) = \mathbf{E}^{inc}(x,y,z) + \mathbf{E}^{ref}(x,y,z)$$

$$= E_0 \mathbf{e}_{10}(x,y)e^{-jk_{z10}z} + RE_0 \mathbf{e}_{10}(x,y)e^{jk_{z10}z} \qquad (4.21)$$

where E_0 denotes the magnitude of the incident wave, R denotes the reflection coefficient, and $\mathbf{e}_{10}$ and k_{z10} are given by

$$\mathbf{e}_{10}(x,y) = \hat{y}\sin\frac{\pi x}{a}, \qquad k_{z10} = \sqrt{k_0^2 - \left(\frac{\pi}{a}\right)^2}$$

with a being the width of the waveguide. From (4.21), the following relationship is obtained

$$\hat{n}\times(\nabla\times\mathbf{E}) = -\hat{z}\times(\nabla\times\mathbf{E}) = -jk_{z10}\mathbf{E}^{inc} + jk_{z10}\mathbf{E}^{ref}$$

$$= jk_{z10}\mathbf{E} - 2jk_{z10}\mathbf{E}^{inc} \qquad (4.22)$$

which can also be written as

$$\hat{n}\times(\nabla\times\mathbf{E}) + \gamma\hat{n}\times(\hat{n}\times\mathbf{E}) = \mathbf{U}^{inc} \qquad (4.23)$$

with

$$\gamma = jk_{z10}, \qquad \mathbf{U}^{inc} = -2jk_{z10}\mathbf{E}^{inc}.$$

Similarly, the field at S_2 can be expressed as

$$\mathbf{E}(x,y,z) = \mathbf{E}^{trans}(x,y,z) = TE_0 \mathbf{e}_{10}(x,y)e^{-jk_{z10}z} \qquad (4.24)$$

where T denotes the transmission coefficient. From this, the following condition is obtained

$$\hat{n} \times (\nabla \times \mathbf{E}) + \gamma \hat{m} \times (\hat{n} \times \mathbf{E}) = 0 \qquad (4.25)$$

valid for the field at S_2.

The relations (4.23) and (4.25) can be regarded as the boundary conditions applicable at S_1 and S_2, respectively. These, together with the well-known governing differential equation for the field within the region of interest and the boundary condition at the waveguide walls, can be solved uniquely using the finite element method. In accordance with the generalized variational principle, the equivalent variational problem is given by

$$\begin{cases} \delta F(\mathbf{E}) = 0 \\ \hat{n} \times \mathbf{E} = 0 \qquad \text{on waveguide wall} \end{cases} \qquad (4.26)$$

where

$$F(\mathbf{E}) = \frac{1}{2} \iiint_V \left[\frac{1}{\mu_r} (\nabla \times \mathbf{E}) \cdot (\nabla \times \mathbf{E}) - k_0^2 \varepsilon_r \mathbf{E} \cdot \mathbf{E} \right] dV$$

$$+ \iint_{S_1} \left[\frac{\gamma}{2} (\hat{n} \times \mathbf{E}) \cdot (\hat{n} \times \mathbf{E}) + \mathbf{E} \cdot \mathbf{U}^{inc} \right] dS + \iint_{S_2} \left[\frac{\gamma}{2} (\hat{n} \times \mathbf{E}) \cdot (\hat{n} \times \mathbf{E}) \right] dS$$

$$(4.27)$$

For the numerical discretization of (4.27), first, the volume V is subdivided into small volume elements and within each element the field is expressed as (4.15). For a discretization of the surface integrals, the planar surfaces S_1 and S_2 are subdivided into small surface elements. Note that the surface and volume discretizations must be compatible; that is, an element edge resulting from the volume discretization must also be an element edge in the surface discretization. Actually, this is always the case because

once the volume is discretized, its surface is also discretized. Within each surface element, we may approximate the field as

$$\hat{n} \times \mathbf{E}^s = \sum_{i=1}^{n_s} \mathbf{S}_i^s E_i^s = \{E^s\}^T \{S^s\} = \{S^s\}^T \{E^s\} \tag{4.28}$$

where the superscript s denotes the surface element number, n_s represents the number of edges comprising the element, and the S_i^s denote the vector basis functions. Obviously, $S_i^s = \hat{n} \times \mathbf{W}_i^s$, where $\mathbf{W}_i^s$ are the vector basis functions that have a unit tangential component at edge i. Substituting (4.15) and (4.28) into (4.27), we obtain

$$F = \frac{1}{2} \sum_{e=1}^{M} \{E^e\}^T [K^e]\{E^e\} + \frac{1}{2} \sum_{e=1}^{M_s} \{E^s\}^T [B^s]\{E^s\} - \sum_{e=1}^{M_{s1}} \{E^s\}^T \{b^s\} \tag{4.29}$$

where M is the total number of volume elements, M_s is the number of surface elements on S_1 and S_2, and M_{s1} is the number of surface elements on S_1 only. Also,

$$[K^e] = \iiint_{V^e} \left[\frac{1}{\mu_r^e} \{\nabla \times \mathbf{W}^e\} \cdot \{\nabla \times \mathbf{W}^e\}^T - k_0^2 \varepsilon_r^e \{\mathbf{W}^e\} \cdot \{\mathbf{W}^e\}^T \right] dV \tag{4.30}$$

$$[B^s] = \iint_{S^s} \gamma S^s \cdot S^s dS \tag{4.31}$$

$$\{b^s\} = \iint_{S^s} \mathbf{S}^s \cdot (\mathbf{U}^{inc} \times \hat{n}) dS. \tag{4.32}$$

Carrying out the summation, replacing the local edge numbers with the corresponding global edge numbers, and applying the Ritz procedure, we obtain the system of equations given by

$$[K]\{E\} = \{b\} \tag{4.33}$$

where $[K]$ is assembled from $[K^e]$ and $[B^s]$, and $\{b\}$ is assembled from $\{b^s\}$. This system can be solved, after imposing the Dirichlet boundary condition to zero out the edge fields coincident with the waveguide wall, for the edge fields inside V as well as on S_1 and S_2.

Once (4.33) is solved for the fields at S_1 and S_2, the reflection and transmission coefficients can be obtained from (4.21) and (4.24), respectively. Specifically, from (4.21), the reflection coefficient can be obtained as

$$R = \frac{\mathbf{E}(x,y,z) - E_0\mathbf{e}_{10}(x,y)e^{-jk_{z10}z}}{E_0 e_{10}(x,y)e^{jk_{z10}z}}\bigg|_{z=z_1} \qquad (4.34)$$

and from (4.24), the transmission coefficient can be obtained as

$$T = \frac{\mathbf{E}(x,y,z)}{E_0 e_{10}(x,y)e^{-jk_{z10}z}}\bigg|_{z=z_2} \qquad (4.35)$$

Ideally, the reflection and transmission coefficients are not functions of (x,y). However, in a numerical solution, when S_1 and S_2 are not placed sufficiently far away from the obstacle one finds that they vary slightly with (x,y). This variation becomes higher when S_1 and S_2 are brought closer to the obstacle. This observation provides a good check on whether S_1 and S_2 are placed far enough from the obstacle.

Better accuracy for the reflection and transmission coefficients can be obtained by utilizing the orthogonality properties of waveguide modes. Since the dominant mode is orthogonal to all other modes, we may take a scalar product of (4.21) and (4.24) with $\mathbf{e}_{10}$ and integrate over the cross section of the waveguide. Doing this, the influence of higher-

order modes excited by the obstacle on the calculation of the reflection and transmission coefficients can be effectively removed. The new expressions for R and T then become

$$R = \frac{2e^{-jk_{z10}z_1}}{abE_0} \iint_{S_1} \mathbf{E}(x,y,z_1) \cdot \mathbf{e}_{10}(x,y)dS - e^{-2jk_{z10}z_1} \qquad (4.36)$$

$$T = \frac{2e^{jk_{z10}z_2}}{abE_0} \iint_{S_2} \mathbf{E}(x,y,z_2) \cdot \mathbf{e}_{10}(x,y)dS. \qquad (4.37)$$

Another good check for the solution accuracy is based on the conservation of power: If the waveguide and obstacle are lossless, the equation $|R|^2 + |T|^2 = 1$ must hold exactly.

4.3.1   Loaded Rectangular Waveguide

Rectangular waveguides are commonly used to facilitate material characterization since they have good operational bandwidth for single-mode propagation, reasonably low attenuation, and good mode stability for the fundamental mode of propagation [17]. In addition, for various bands of operation, appropriate standard waveguides are ubiquitous in a well-equipped electromagnetic test facility. Consider a rectangular waveguide with a TE_{10} mode wave incident on a sample at $z = 0$ as shown in Figure 4.3. The waveguide has fixed dimensions for width $-a/2 \le x \le a/2$ and height $y = b$, where the width a is in general greater than twice the height b. The length L of the sample waveguide region (S) may vary. The sample, which has one fixed dimension, height $y = b$, and two varying dimensions, width $-d/2 \le x \le d/2$ and length $z = L$, will be centered in the waveguide at $x = 0$.
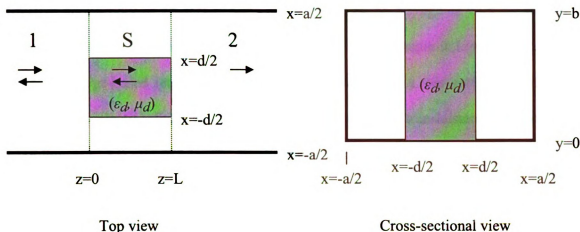
| | | x=a/2 | | | y=b |
| | | | | | |

Figure 4.3 Loaded rectangular waveguide.

Andrew Bogle's thesis [31] demonstrated, through the use of a modal-analysis technique, how using a partially filled rectangular waveguide cross-section allows for better transmission responses to extract the complex constitutive parameters. In this work, before testing any samples experimentally, a few simple validation tests were done to verify the extraction process. The first test involves reversing the extraction process to generate scattering parameters for the special case of a completely filled waveguide cross-section. This special case allows the generated scattering parameters from mode-matching method to be compared with results for well known transmission line theory and experimentally measured data. Here, in order to test the numerical code developed with finite element method for electromagnetic model, the completely filled waveguide case is studied with the FEM code and is compared with mode-matching results from [31].

The configuration studied consists of the standard X-band rectangular waveguide (a = 0.9 inch and b = 0.4 inch), and a sample of lossless, non-magnetic acrylic with

effective permittivity of 2.5 that fills the cross-section of the waveguide with $d = a$. The total length of the waveguide is 3cm while the length of the sample is L = 0.75 cm. The FEM with edge-based tetrahedral elements described above in this section is used to calculate the electric field as well as the reflection and transmission coefficients according to (4.34) and (4.35). The results are compared with data from [31] using the mode-matching method for the frequency range of 8 – 12 GHz and shown in Fig. 4.4. It can be seen that a good agreement is achieved.
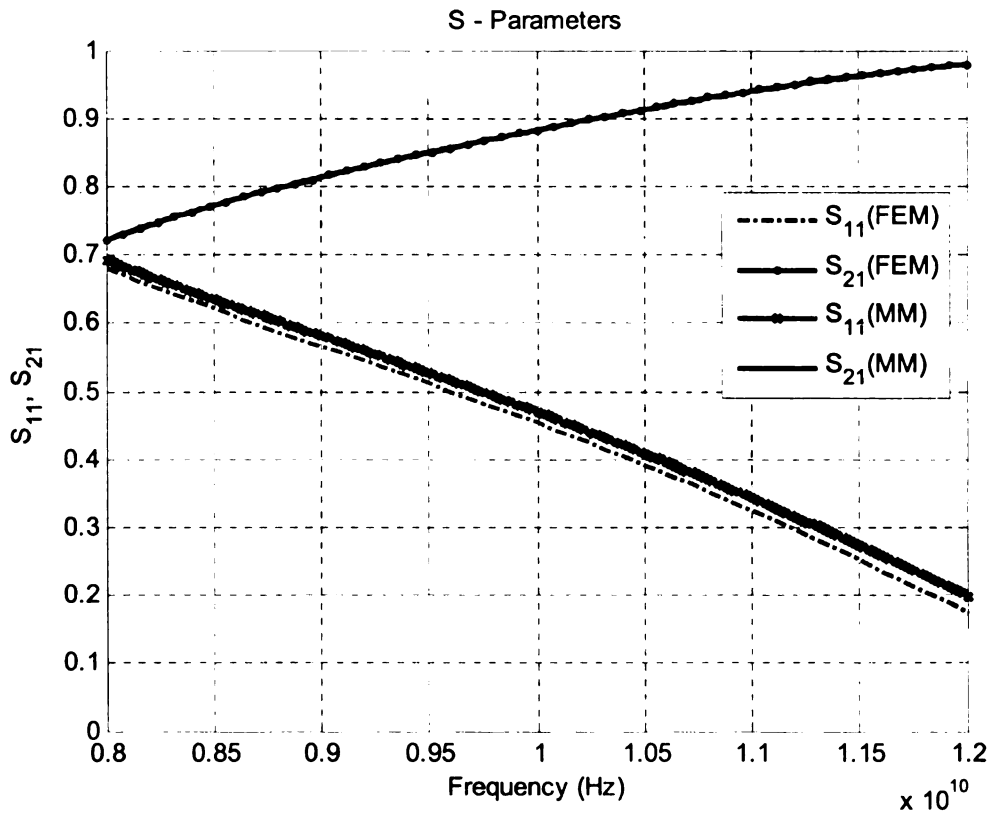

Figure 4.4 S-parameters for the completely filled waveguide.

4.3.2   Waveguide Bandpass Filters

The high unloaded Q-factor of TE_{011}-mode in cylindrical cavity is very attractive for the realization of low-loss narrow-band filters at millimeter wavelengths. Direct coupled filters employing this kind of resonators can be designed to have a very selective passband with steep skirts, together with a very low midband insertion loss. One further advantage is the higher midband pulse power capacity, when compared to other waveguide filters.

In [32], a mode-matching technique was presented to analyze accurately this kind of filters. That procedure accurately took into account the effects of the thick coupling apertures, the irises angular offset 2θ, the spurious responses and the higher mode interaction between adjacent resonators, overcoming the limitations of available approximate models [33], [34].

The main building block of the TE_{011}-mode bandpass filter is the cylindrical resonator shown in Fig. 4.5, coupled both with the external rectangular waveguides and with the adjacent cavities through two rectangular apertures (coupling irises) which are placed on the cavity sidewall with an angular offset equal to 2θ. In this part, the FEM code developed herein is checked with the results from mode-matching method [32] for a simple case where $2\theta = 180°$.
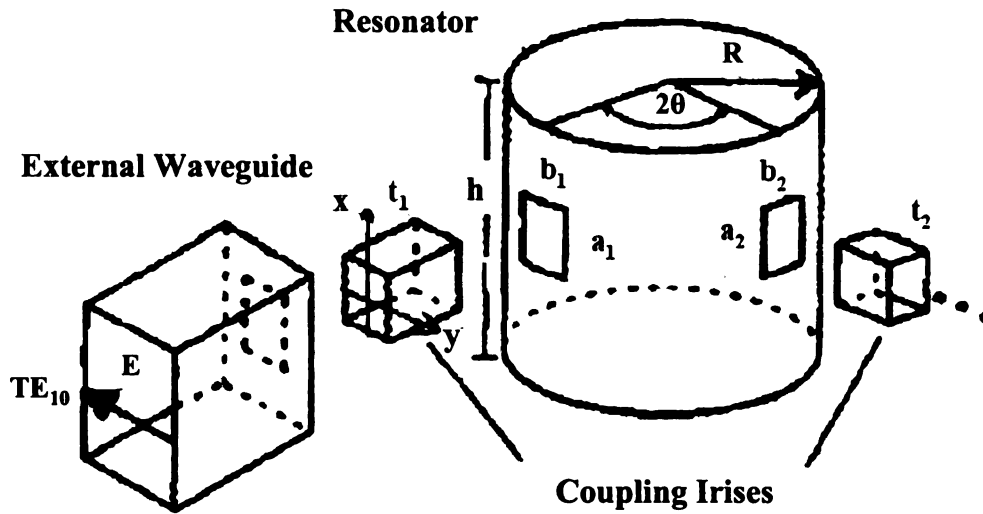
Figure 4.5 Schematic view of the TE_{011}-mode bandpass filter [32].

The studied configuration has the cavity with diameter D = 34 mm and height h = 20.5 mm, coupled by two identical irises with dimensions a_i = 8 mm, b_i = 4 mm and t_i = 3 mm to an external R120 waveguide (a_{w1} = a_{w2} = 19.05 mm, and b_{w1} = b_{w2} = 9.525 mm) forming an angle 2θ = 180°. For the FEM code, the geometry and mesh information are extracted from FEMLAB [35], as shown in Fig. 4.6. Calculated values of S_{21} using the FEM code is shown in Fig. 4.7, while the measured and computed S_{21} with mode-matching from [32] are shown in Fig. 4.8 for a wide frequency band. It can be seen that a good agreement with each other is obtained.
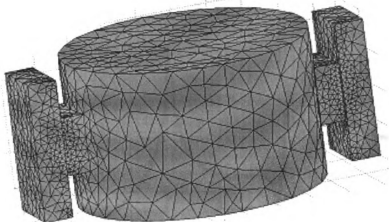
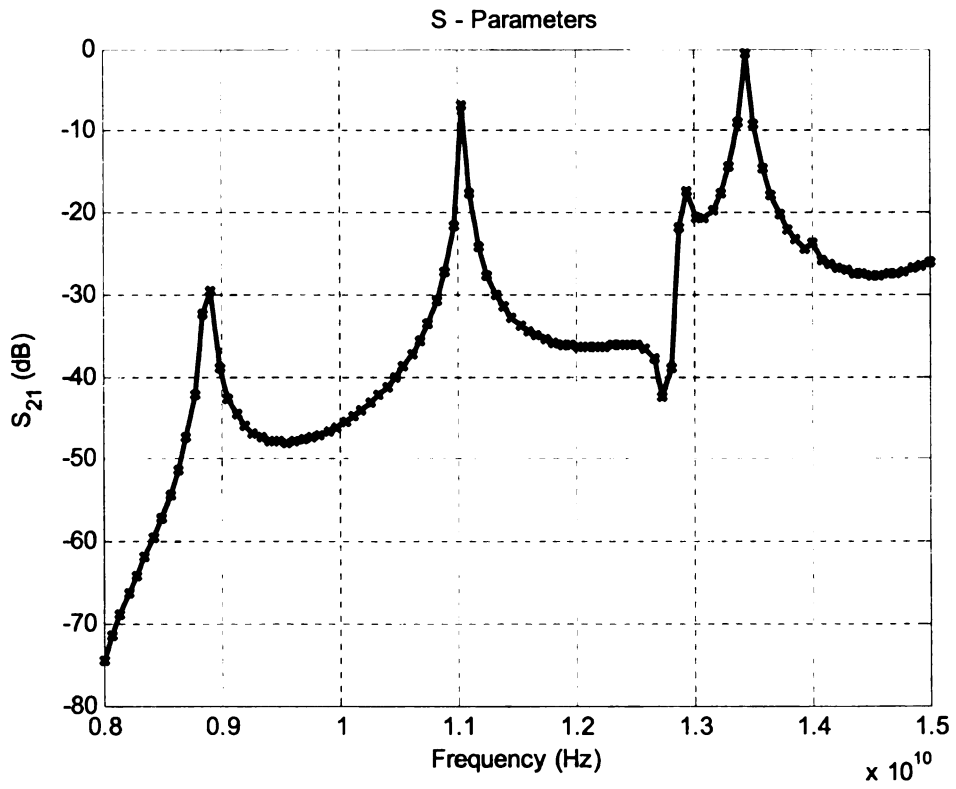Figure 4.6 Meshed geometry of the bandpass filter.

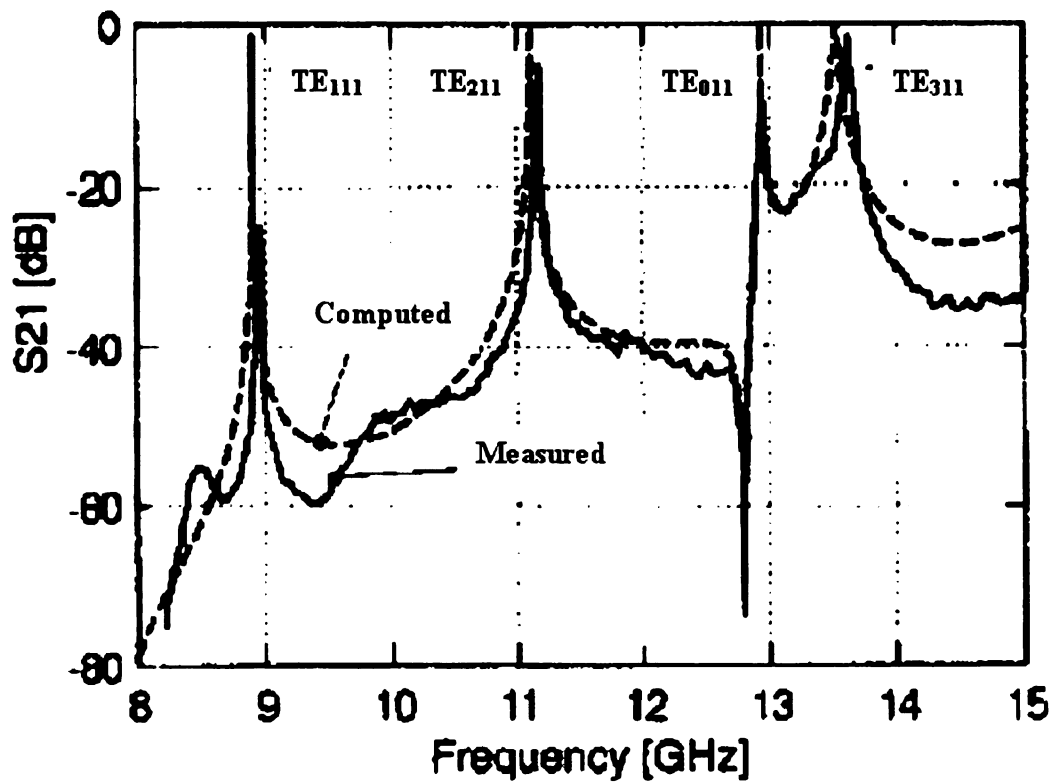Figure 4.7 Calculated magnitude of S_{21} for the bandpass filter with FEM.

Figure 4.8 Magnitude of S_{21} for the bandpass filter from [32].

CHAPTER 5 CETK MULTIPHYSICS MODELING

5.1 Overview

Coupled EM-thermal problems have been studied for various applications [36-46], for example, microwave drying of capillary porous materials [36], microwave epoxy curing [37], microwave processing of foods [38] [39], microwave sintering of ceramics [40], microwave heating of laminar material [41], and RF heating for non-ablative cutaneous therapy [42]. The multiphysics numerical models in these papers were implemented using either FDTD or FEM to simulate the time-marching process, considering both electromagnetic and heat transfer effects. Among these efforts, articles [39] and [40] include the consideration of the sample dielectric property variation as function of temperature during heating process, and update the material property from time to time when necessary. Article [37] reported a two-dimensional EM-thermal modeling of epoxy curing process for two operating frequencies, but did not include the reaction heat due to the thermoset curing in the energy balance equation, which is very significant after the curing process starts.

In this chapter, a self-consistent 3D marching-in-time multiphysics model is presented, which includes electromagnetic field distribution, microwave power absorption, heat transfer, and polymer curing kinetics. Temperature-dependent permittivity and curing kinetics for diglycidyl ether of bisphenol A (DGEBA) / diaminodiphenyl sulfone (DDS) based on experimental data are explicitly included in the model. Edge-based FEM is implemented for electromagnetic model to ensure the tangential continuity of electric field and divergence-free condition for source free region, while node-based FEM is used in thermal model to solve for the temperature distribution.

The numerical results can be used to determine the time-dependent temperature distribution and curing profile across the polymer sample, as well as the electromagnetic field distribution within the cavity applicator. With the help of this numerical model, robust control strategies can be developed for the polymer curing process. The numerical results are compared with the measured data and a good agreement is achieved.

5.2 Energy Balance Equation

During the epoxy thermoset curing process, the energy balance for the material being processed within the applicator is governed by the following equation

$$\rho C_p \frac{\partial T}{\partial t} = P + \nabla \cdot \left[\breve{k}(T) \cdot \nabla T \right] + \rho \frac{\partial \alpha}{\partial t} (-\Delta H_r) \qquad (5.1)$$

where ρ is density (kg/m^3), C_p is heat capacity (J/kg/K), T is temperature (K), t is time (second), $\breve{k}$ is the anisotropic thermal conductivity tensor (W/K/m), α is exten-of-cure, and $-\Delta H_r$ is reaction heat (J/kg).

On the right hand side in (5.1), P is microwave power absorption rate (W/m^3) inside the epoxy sample, and is expressed in terms of the electric field strength and the permittivity as below:

$$P = \frac{1}{2} \omega \varepsilon_0 \varepsilon_r''(\alpha, T) \mathbf{E} \cdot \mathbf{E}^* \qquad (5.2)$$

where $\mathbf{E}$ is the electric field strength inside the epoxy material (V/m), ω is the radial frequency (rad/sec), $\varepsilon_0 = 8.854 \times 10^{-12}$ farad/m is the free-space permittivity. ε'' is the effective relative loss factor and is the function of local temperature and extent-of-cure for epoxy sample. More details will be discussed in section 5.4. The electric field is

determined by solving the vector wave equation using finite element method, and will be presented in details in section 5.5.

The term $\nabla \cdot \left[\bar{k}(T) \cdot \nabla T \right]$ represents the conduction heat transfer, which is the primary heat transfer mechanism, inside the epoxy sample. The free convection boundary condition is applied on all surfaces, and will be discussed in detail in section 5.6.

Since the epoxy thermoset curing process is exothermic, the chemical reaction heat is included in the energy balance equation (5.1), which is the term $\rho \dfrac{\partial \alpha}{\partial t} \left(-\Delta H_r \right)$. Each thermoset system has a particular extent-of-cure vs. time characteristic that is also dependent on temperature. More details on the curing kinetics model will be presented in section 5.3.

Hence, the energy balance equation (5.1) readily demonstrates the interrelationship between electromagnetic, composition, thermal, and kinetic modeling. The critical aspect of the modeling approach used herein relies on the fact that electromagnetic interactions occur much faster, $O(\text{ns})$, than thermal effects, $O(\mu\text{s})$, or the kinetic/composition effects, $O(\text{s})$. Hence, the electromagnetic analysis can be performed with an efficient steady-state analysis method whose results are used in solving the energy balance equation for heat transfer problem. Specifically, in the heat transfer model, after the node-based FEM for spatial variations is performed, a first-order ordinary differential equation (ODE) system is obtained and the finite difference scheme for temporal variations will be used for the time-marching process. The dielectric property of the epoxy sample is updated with the new temperature and extent-of-cure, then the electric field will be solved again to get the new power absorption rate and solve for the heat transfer equation. This process is repeated and the temperature profile can be

obtained across the sample for any given time. More details on the procedure of this process model will be given in section 5.6.

5.3 Curing Kinetics

For polymer curing, existing reaction kinetics models include an nth-order reaction model [6-7] and an autocatalyzed reaction model [8-10]. The curing reactions for an epoxy are characteristic of autocatalyzed reactions. The reactions between amines and epoxide are autocatalyzed by the hydroxide group formed in the reactions. The generalized form of the autocatalyzed reaction kinetics for epoxy curing was derived from the reaction kinetic mechanism [11]. The extent of reaction can be measured experimentally as a function of time and temperature. The reaction constants and parameters can be determined with regression of experimental data.

Reaction kinetics for a simple epoxy resin, diglycidyl ether of bisphenol A (DGEBA) / diaminodiphenyl sulfone (DDS), at 145°C, 165°C, and 185°C, has been studied at Michigan State University [47]. The reaction heat, $-\Delta Hr$, was 413.9±5.1 J/g as determined with Differential Scanning Calorimetry (DSC). The curing reactions for an epoxy are characteristic of autocatalyzed reactions. The reactions between amines and epoxide are autocatalyzed by the hydroxide group formed in the reactions. The following phenomenological model was used to describe the autocatalyzed reaction for a stoichiometric reactant mixture:

$$\frac{d\alpha}{dt} = (k_1(T) + k_2(T)\alpha^m)(1 - \alpha)^n \tag{5.3}$$

54

where k_1 is the non-catalytic polymerization reaction rate constant, k_2 is the autocatalytic polymerization reaction rate constant, m is the autocatalytic polymerization reaction order, and n is the non-catalytic polymerization reaction order.

The epoxy was cured with microwave power in a cylindrical single mode cavity. The extent of reaction was measured experimentally as a function of time and temperature. The reaction constants and parameters were determined with regression of the experimental data and presented in Table 5.1 [47]. Using these parameters, the extent of reaction can be regenerated with the kinetics model. Fig. 5.1 shows the experimental data (markers) and the calculated values (lines) [47]. The kinetic model fits the experimental data very well. Fig. 5.2 shows the calculated time derivative of extent-of-cure ($d\alpha/dt$) as a function of extent-of-cure for different heating temperature, which will be used in the numerical model on the right hand side (RHS) considering reaction heat. In the code, the extent-of-cure distribution across the sample can be obtained by the integration of the time derivative of extent-of-cure for the timestep locally for each tetrahedral element. The time derivative of extent-of-cure will be updated during curing process for each element with the local heating temperature and extent-of-cure.

Table 5.1 Epoxy curing reaction constants and parameters

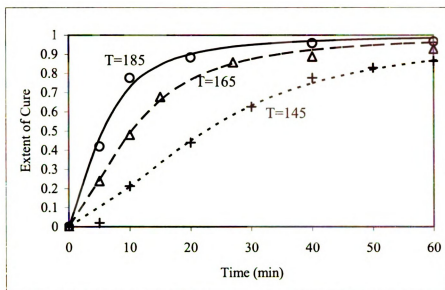|	Microwave Curing at 145°C	Microwave Curing at 165°C	Microwave Curing at 185°C
Non-catalytic reaction order n	1.57		
Autocatalytic reaction order m	0.94		
Non-catalytic reaction rate constant k_1	0.016	0.040	0.089
Autocatalytic reaction rate constant k_2	0.084	0.16	0.24

Figure 5.1 Extent-of-cure vs. time and temperature for DGEBA/DDS (markers represent

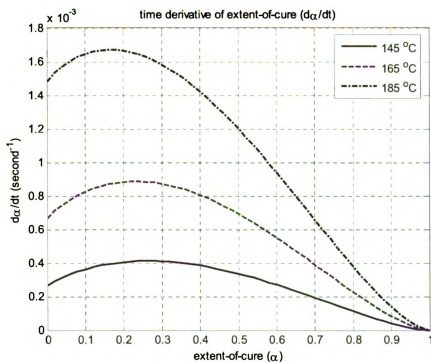experimental data and lines represent calculated data from the model).

Figure 5.2 Time derivative of extent-of-cure vs. extent-of-cure.

5.4 Dielectric Properties

The work on assessing the dielectric properties of the curing systems of DGEBA epoxy resin with the curing agent DDS as a function of temperature and extent-of-cure at 2.45 GHz has been primarily conducted by Dr. Liming Zong at MSU [20, 48]. Generally, the real and the imaginary parts of the complex permittivity increase as the temperature increases and decrease as the extent-of-cure increases. The two reasons accounting for the evolution of the dielectric quantities are a decrease in the number of the dipolar groups in the reactants and an increase in the viscosity. The Davidson-Cole model can be used to describe the experimental data. The details will be discussed below in this section.

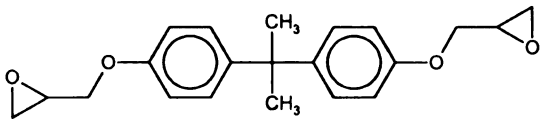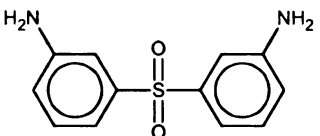The complex permittivity of materials is expressed as follows:

$$\varepsilon^* = \varepsilon' - j\varepsilon'' = \varepsilon_0(\varepsilon'_r - j\varepsilon''_r) \qquad (5.4)$$

where ε' is the dielectric constant, ε'' is the dielectric loss factor, ε_0 (=8.85 x 10^{-12} F/m) is the free-space permittivity, ε'_r is the relative dielectric constant, and ε''_r is the relative dielectric loss factor. Although ε'_r is referred to as the dielectric constant in many papers, it is a function of temperature, pressure, humidity, and other conditions. For convenience, specifically, in this section hereafter, ε' refers to ε'_r while ε'' refers to ε''_r.

The epoxy resin used in this study was DGEBA and the curing agent is DDS. The chemical structures and properties of DGEBA and DDS are shown in Table 5.2. Stoichiometric DGEBA and DDS were mixed before each experiment. A single-frequency microwave processing and diagnostic system was used to heat the epoxy materials and to assess the dielectric properties. The heating mode was TM $_{012}$ and the frequency was 2.45 GHz. The curing temperature was 145°C. After heating, the single frequency microwave curing system was switched to become a low-power swept

frequency diagnostic system. Measurements of temperature and dielectric properties using the swept frequency method were made during free convective cooling of the samples. The cooled samples were analyzed with a Differential Scanning Calorimeter (DSC) to determine the residual heat of reaction per gram and, thus, the extents of cure. More details on the experimental system, sample preparation, and measurement procedures can be found in [48], or section 5.7 in this chapter.

Table 5.2 Properties of the epoxy resin and the curing agent

Name	Chemical Structure	Epoxy/amine equivalent weight	Density at 25°C (g/ml)
DGEBA		171-175	1.16
DDS		62	1.33

The measured dielectric constant and dielectric loss factor of reacting DGEBA/DDS epoxy resins at different temperatures for different extent-of-cure states are shown in Figure 5.3. The extent-of-cure was calculated from DSC data, which are shown in Table 5.3. Due to the non-uniformity of microwave heating, a distribution of extent-of-cure exists in the samples. From Figure 5.3, it is found that both dielectric constant and dielectric loss factor increase as the temperature increases and decrease as the curing reaction proceeds.
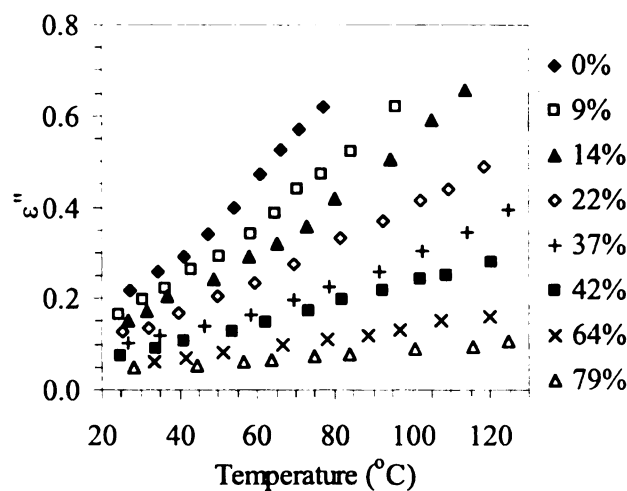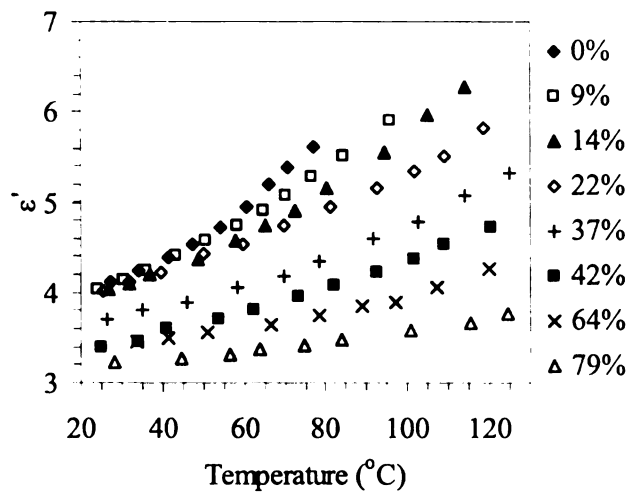
Figure 5.3 Measured dielectric properties for the DGEBA/DDS.

Table 5.3 DSC results of the curing DGEBA/DDS system

Reaction Heat (J/g)	432	387	395	324	249	168	203	72
	448	436	415	350	253	299	153	109
	419	403	360	362	269	262	58	63
	439	370	330	370	294	222	57	64
	429	365	363	290	308	297	319	157
Average	433	392	372	339	275	250	158	93
Extent of Cure	0%	9%	14%	22%	37%	42%	64%	79%
Standard Error	1%	3%	3%	3%	3%	6%	11%	4%

The stoichiometric curing reaction of epoxy resins with amines is illustrated in Figure 5.4 [49, 50]. In the first step, an epoxy group reacts with a primary amine to form a hydroxyl group and a secondary amine. In the second step, the formed secondary amine reacts with another epoxy group to produce a hydroxyl group and a tertiary amine. The progress of the reaction is defined in terms of extent-of-cure. The viscosity of the reacting systems rise as the polymerization goes on and two distinguishable transitions, i.e. the gelation and the vitrification, were observed.
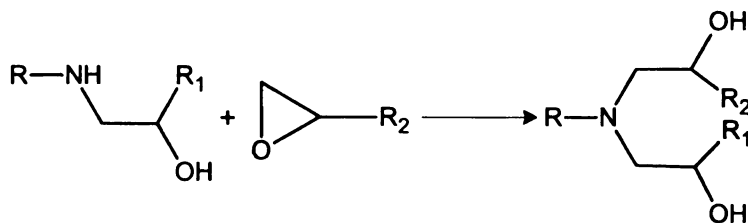
Step 1
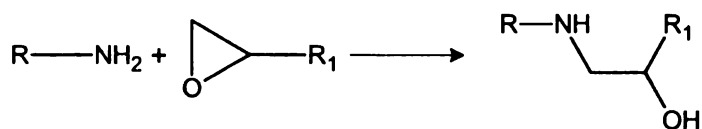
Step 2

Figure 5.4 DGEBA resin curing mechanism.

The unreacted epoxy groups, -O-, and amine groups, $-NH_2-$, within the reaction system are the main driving forces for the apparent combined γ relaxation observed in this study. The disappearance of the epoxy and amine groups during the reaction is one reason accounting for the changes of the dielectric properties. An increase in the viscosity during the reaction is the other reason. The increasing viscosity of the reacting systems

60

should hinder the mobility of the dipolar groups associated with the relaxation and cause the relaxation time to increase.

The Davidson-Cole model [51] can be used to describe the dielectric behavior of DGEBA epoxy resins:

$$\varepsilon * -\varepsilon_\infty = \frac{(\varepsilon_0 - \varepsilon_\infty)}{(1 + j\omega\tau)^n}$$

$$\varepsilon' = \varepsilon_\infty + \frac{(\varepsilon_0 - \varepsilon_\infty)\cos(n\theta)}{(1 + (\omega\tau)^2)^{\frac{n}{2}}}$$

(5.5)

$$\varepsilon'' = \frac{(\varepsilon_0 - \varepsilon_\infty)\sin(n\theta)}{(1 + (\omega\tau)^2)^{\frac{n}{2}}}$$

$$\theta = \text{arc} \tan(\omega\tau)$$

where τ is the relaxation time in second; ε_0 is the static frequency dielectric constant; ε_∞ is the high frequency dielectric constant, and n is the shape parameter with a range of $0 \leq$ n≤ 1.

The dominant γ relaxation time should fit the Arrhenius rate law [52]:

$$\tau = A \times e^{\left(\frac{E_a}{RT}\right)}$$

(5.6)

where E_a is the activation energy in J/mol, R (=8.314 J/mol·K) is the molar gas constant, T is the temperature in K, and A is the relaxation time in the high temperature limit in second.

The values of the parameters, n, ε_∞, and E_a, and a relation between (ε_0-ε_∞) and A, can be calculated using equations (5.5) and (5.6) [48], while the values of (ε_0-ε_∞) was taken from the literature [53] and then A was determined. Specifically, all the values of

the parameters for the curing DGEBA/DDS system with different extent-of-cure are listed in Table 5.4. Figure 5.5 shows the comparison of the experimental and calculated data of the reacting DGEBA/DDS system, where the curves represent the calculated data from the Davidson-Cole expression and the markers represent experimental data. It can be shown that the data from Davidson-Cole model fit the measured data very well within the temperature range between 20 °C and 130 °C (note that the thermoset curing for DGEBA/DDS starts once the temperature goes beyond about 125 °C).
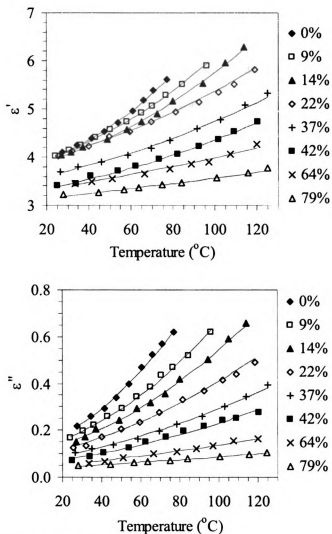

Figure 5.5 Comparison between the experimental and calculated permittivity of DGEBA/DDS.

Table 5.4 Values of the parameters for the curing DGEBA/DDS system

Extent of Cure	n	ε_0	ε_∞	$(\varepsilon_0 - \varepsilon_\infty)$	E_a (kJ/Mol)	A (s)
0%	0.17	9.10	3.29	5.81	110	4.2E-25
9%	0.15	8.67	3.33	5.34	110	1.7E-24
14%	0.14	8.47	3.30	5.16	112	2.1E-24
22%	0.13	8.12	3.43	4.69	107	5.2E-23
37%	0.11	7.45	3.11	4.34	119	8.6E-24
42%	0.10	7.19	2.89	4.30	133	7.1E-25
64%	0.08	6.24	2.93	3.31	129	5.4E-23
79%	0.07	5.57	2.73	2.83	121	7.2E-20

In the numerical code for the process model, the complex permittivity of the epoxy sample will be updated with the local temperature and extent-of-cure as the microwave heating is proceeding. In order to get the values of the complex permittivity that are beyond the temperature range of the measured data and to do the interpolation between different extents of cure, the dielectric constant and loss factor are calculated for the temperature range of 0 °C and 300 °C based on Davidson-Cole model, and shown in Fig. 5.6 and 5.7, respectively.

However, it is found that the dielectric loss factor calculated from Davidson-Cole model is not accurate for relatively high temperature, say, beyond 130°C for DGEBA/DDS in this case. Considering Fig. 5.7, since interpolation is necessary for the values of the dielectric loss factor between different extents of cure in the numerical model, at the high temperature the values of the loss factor will change very abruptly. This is not the real situation as observed from experimental value obtained in [54], where the loss factor changes smoothly.

In order to overcome this problem, the values of the dielectric loss factor calculated from Davidson-Cole model are modified such that they follow the same trend as the dielectric constant and are shown in Fig. 5.8. Specifically, after the dielectric loss

factor reaches its maximum value for each extent-of-cure, it remains constant at higher temperature. In practice, it is very difficult and sometimes even impossible to obtain accurate measured data at high temperature for the low extent-of-cure, since the curing is actively going on at high temperature and both the dielectric loss factor and extent-of-cure keep changing during the measurement. Therefore, even this modified model may not be true in practice; however, it gives a very good way to do the interpolation and to provide reasonable approximation values for the loss factor, and as will be seen in section 5.8, good results are obtained based on this modified Davidson-Cole model. It is hoped more experimental efforts and theoretical research can be done in the near future to provide more accurate model on the complex permittivity for epoxy resins.
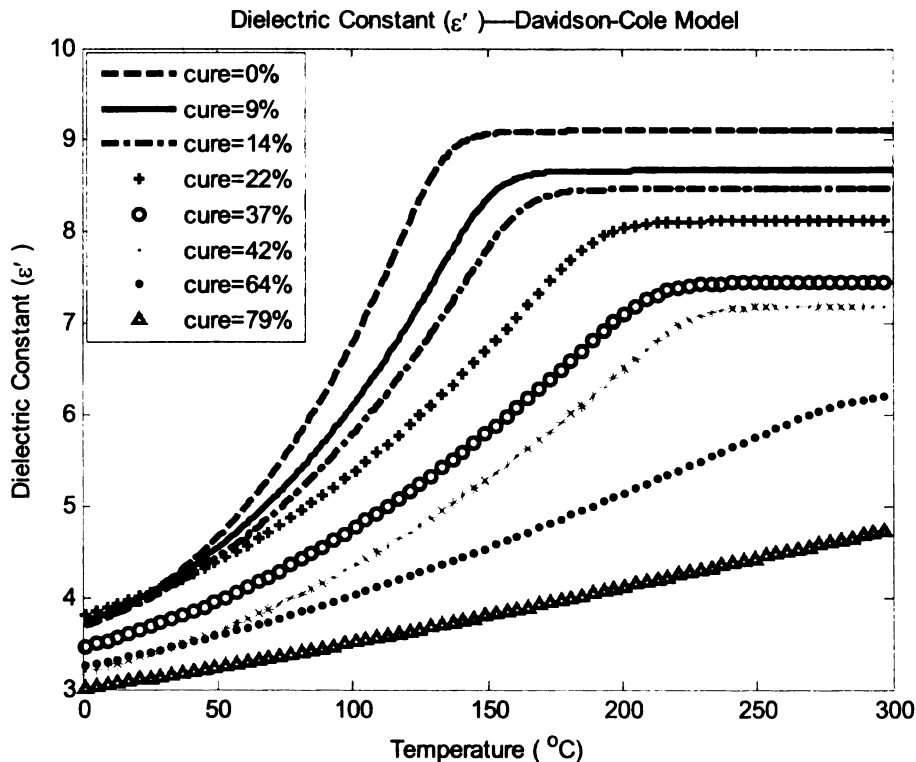

Figure 5.6 Calculated dielectric constant for DGEBA/DDS based on Davidson-Cole model for a wider temperature range.
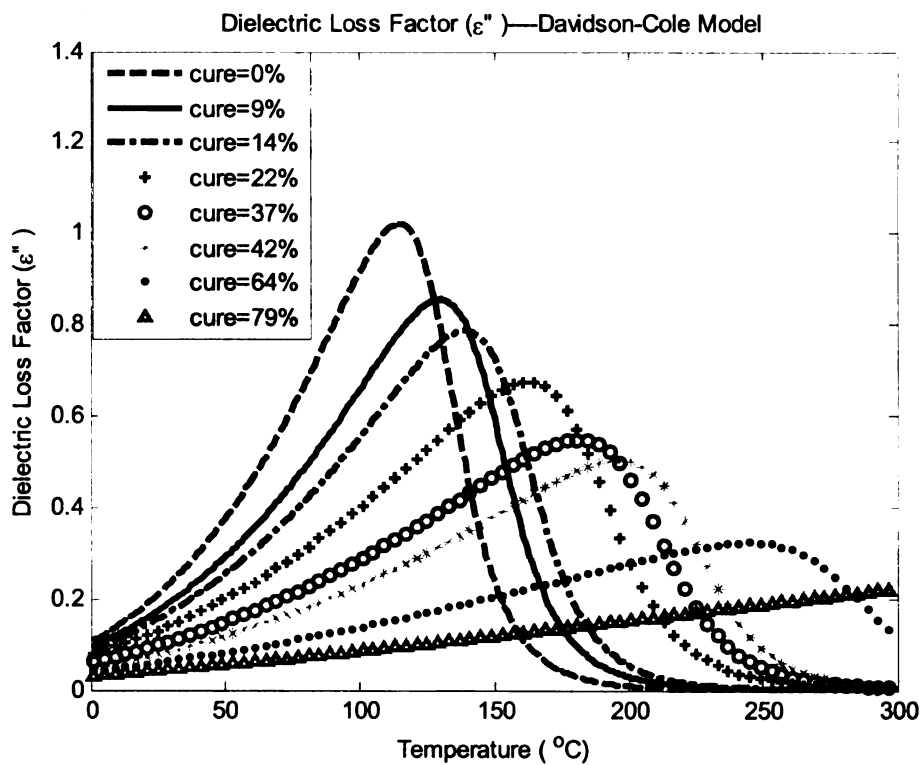
Figure 5.7 Calculated dielectric loss factor for DGEBA/DDS based on Davidson-Cole
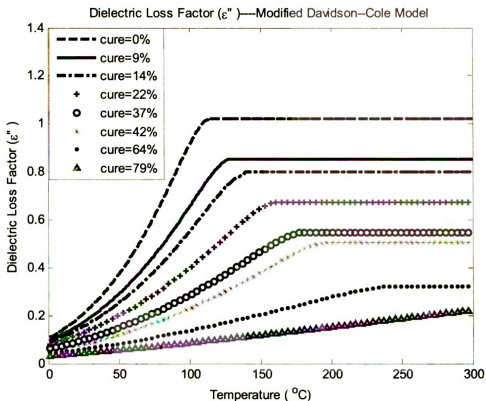
model for a wider temperature range.

Figure 5.8 Calculated dielectric loss factor for DGEBA/DDS based on modified

Davidson-Cole model for a wider temperature range.

5.5 Electromagnetic Model

The edge-based finite element method with tetrahedral elements for the applicator and polymer sample is used since this method offers a high degree of geometrical and electrical fidelity. In particular, the spatial variation in permittivity can readily be accommodated and by using "snapshots-in-time", time-dependant thermal and composition influences on the local permittivity can be included in the model. Recall that such quasi-stationary analysis approaches are valid since the evolution of thermal and composition effects are relatively slow compared to the rate of electromagnetic field propagation within the applicator.

The finite element method is well-suited for resonant cavity simulation since it can incorporate the presence of a sample as well as determine the response of the system to single frequency excitation in an efficient manner. Once the fields are determined throughout the cavity for a given excitation, local power absorption rate can be determined for the heat transfer model.

Specifically, the configuration of the applicator loaded with an epoxy sample in the numerical model is shown in Fig. 5.9, with an enlarged view at the epoxy sample on the right side in the figure. The applicator is a coax-fed single-mode cylindrical cavity with the diameter of 15.24 cm and the height of 16.0 cm, such that TM_{012} mode is excited inside the cavity at 2.45 GHz. The pattern of the total electric field distribution for TM_{012} mode is shown in Fig. 5.10. The epoxy sample is centered at the middle of the cavity, where the electric field strength is the strongest. The diameter of the epoxy sample is 1.0 cm and the height is 2.7 cm. The sample is held by a Teflon holder with the wall thickness of 0.2 cm and the base thickness of 0.3 cm. The Teflon has the complex permittivity $\varepsilon_r^* = 2.1 - j0.0004$.
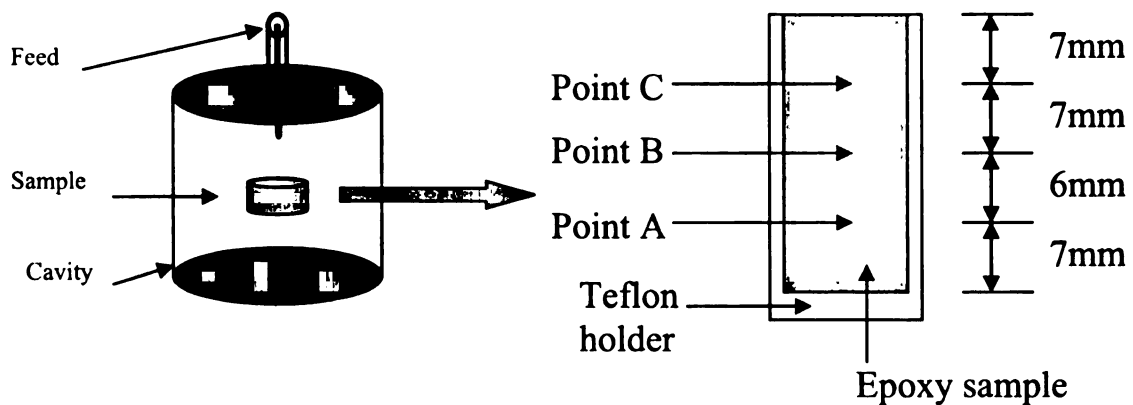

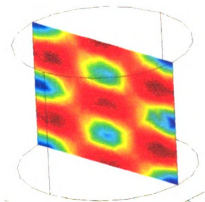Figure 5.9 Coax-fed single-mode cavity with the epoxy sample loaded.

Figure 5.10 Pattern of the total electric field distribution for TM$_{012}$ mode inside the

cavity.

Regarding the mesh generation for computational purpose by finite element method, SKY/Mesh2 mesh generator [55] was used to get the 2D mesh with triangular elements. The triangular elements are extruded to form prism elements, and the latter elements are subdivided to get tetrahedral elements [56], which provide increased flexibility on geometry.

The electric field, inside the cavity and at each point within the epoxy sample being processed, can be computed using edge-based finite element method. The set of finite element equations, derived from the vector wave equations and using Galerkin testing, is given by

$$\sum_{j=1}^{N} E_j \int_V \left[\frac{\nabla \times \mathbf{W}_i \cdot \nabla \times \mathbf{W}_j}{\mu_r} - k_0^2 \varepsilon_r^* \mathbf{W}_i \cdot \mathbf{W}_j \right] dV = -j k_0 Z_0 \int_V \mathbf{W}_i \cdot \mathbf{J}^{\text{int}} dV$$

(5.7)

where the vector testing function is denoted by $\mathbf{W}_i$ and the vector expansion function for the total electric field is denoted as $\mathbf{W}_j$. Tetrahedral elements with edge-based basis functions, which have been discussed in chapter 4, are used to solve for the electric field. The term on the right hand side (RHS) accounts for the excitation from coaxial cable at the top, in the way demonstrated by [21]. The Dirichlet boundary condition, $\hat{n} \times \mathbf{E} = \mathbf{0}$ where $\hat{n}$ is the surface normal, is applied on the inner conducting surfaces of the cylindrical cavity.

Regarding the data storage scheme for the sparse matrices generated from assembling, compressed sparse row (CSR) format [57] was used to save the memory and CPU time. For the solving process, a biconjugate gradient (BiCG) iterative solver [58] was used to solve the linear equations.

Once the values of the electric field are obtained, the power absorption rate within the epoxy sample can be obtained with the expression

$$P = \frac{1}{2}\omega\varepsilon_0\varepsilon_r''(\alpha,T)\mathbf{E} \cdot \mathbf{E}^*$$
(5.8)

Since the complex permittivity of the DGEBA/DDS is the function of the local temperature and extent-of-cure, both the dielectric constant and the loss factor keep changing during the thermoset curing process. Therefore, in order to simulate the process accurately, the material property must be updated. Specifically, the complex permittivity of the epoxy sample, in the system equation (5.7) and the power absorption rate expression (5.8), must be updated with an appropriate timestep in the time-marching process. This procedure will be discussed in more details in section 5.6.

5.6 Heat Transfer Model

In the heat transfer model, node-based FEM with tetrahedral elements is used since the temperature is a scalar variable. The temperature distribution can be obtained by solving the energy balance equation (5.1), which includes microwave power deposition, heat transfer and heat generation due to thermoset curing. After the node-based FEM for spatial variations is performed, a first-order ordinary differential equation (ODE) system is obtained and the finite difference scheme for temporal variations will be used for time-marching process.

Recall the energy balance equation for the epoxy sample and Teflon holder

$$\rho C_p \frac{\partial T}{\partial t} = P + \nabla \cdot \left[\tilde{k}(T) \cdot \nabla T \right] + \rho \frac{\partial \alpha}{\partial t} (-\Delta H_r) \tag{5.9}$$

in the numerical model, the parameters of the material properties for DGEBA/DDS epoxy resins and the Teflon holder are listed in Table 5.5. For convenience, there is no difference in symbols between the epoxy resins and the Teflon holder.

Table 5.5 Parameters of the material properties in the heat transfer model

Parameter	Symbol	Value	Unit
DGEBA/DDS			
Density	ρ	1160.0	kg/m^3
Heat capacity	C_p	200.0	J/kg/K
Thermal conductivity	k	0.24	W/m/K
Teflon			
Density	ρ	2190.0	kg/m^3
Heat capacity	C_p	995.0	J/kg/K
Thermal conductivity	k	0.24	W/m/K

Although the same mesh from the electromagnetic model is used, only the region consisting of the epoxy resins and the Teflon holder needs to be considered for the heat transfer problem. After applying Galerkin testing (assuming diagonal tensor for thermal conductivity), (5.9) becomes

$$\int_V \left[k_x \frac{\partial N_j}{\partial x} \frac{\partial N_i}{\partial x} \{T\} + k_y \frac{\partial N_j}{\partial y} \frac{\partial N_i}{\partial y} \{T\} + k_z \frac{\partial N_j}{\partial z} \frac{\partial N_i}{\partial z} \{T\} \right] dV$$

$$+ \int_V \rho C_p N_i N_j \frac{\partial \{T\}}{\partial t} dV + \int_S h N_i N_j \{T\} dS \qquad (5.10)$$

$$= \int_V \frac{1}{2} \omega \varepsilon_0 \varepsilon_r''(\alpha, T) \mathbf{E} \cdot \mathbf{E}^* N_i dV + \int_S h T_\infty N_i dS + \int_V \rho \frac{\partial \alpha}{\partial t} (-\Delta H_r) N_i dV$$

In the above equation, the natural air free convection boundary condition is already applied between the Teflon/air or epoxy/air interfaces, as

$$-(\breve{k} \cdot \nabla T) \cdot \hat{\mathbf{n}} = h(T - T_\infty) \qquad (5.11)$$

where $\breve{k}$ is the anisotropic thermal conductivity tensor, $\hat{\mathbf{n}}$ is the surface normal, and T_∞ (= 20 °C) is the surrounding air temperature. The convective heat transfer coefficient h is a very important parameter and needs to be considered very carefully. Typical value of h for natural air free convection ranges between 5—25 W/m²/K. A parametric study on h will be done in section 5.8 to see the influence of its variation on numerical results.

For each tetrahedral element, the elemental matrix is given by

$$[C^e] \left\{ \frac{dT^e}{dt} \right\} + [K^e] \{T^e\} = \{Q^e\} \qquad (5.12)$$

where

$$C_{ij}^e = \int_V \rho C_p N_i N_j dV$$

$$K_{ij}^e = \int_V \left[k_x \frac{\partial N_j}{\partial x} \frac{\partial N_i}{\partial x} + k_y \frac{\partial N_j}{\partial y} \frac{\partial N_i}{\partial y} + k_z \frac{\partial N_j}{\partial z} \frac{\partial N_i}{\partial z} \right] dV + \int_S h N_i N_j dS$$

$$Q_i^e = \int_V \frac{1}{2} \omega \varepsilon_0 \varepsilon_r''(\alpha,T) \mathbf{E} \cdot \mathbf{E}^* N_i dV + \int_S h T_\infty N_i dS + \int_V \rho \frac{\partial \alpha}{\partial t} (-\Delta H_r) N_i dV$$

$$(5.13)$$

Performing the integrations and assembling, the linear system representing the first-order ordinary differential equations (ODE) is given as

$$[C] \left\{ \frac{dT}{dt} \right\} + [K]\{T\} = \{Q\} \qquad (5.14)$$

The finite difference scheme known as the θ-method [59] is used to solve the system and to obtain the updated temperature for the sample and Teflon holder. The dielectric property of the epoxy sample is updated with the new temperature and extent-of-cure, then the electric field will be solved again with edge-based FEM to get the new power absorption rate and solve for the heat transfer equation. This process is repeated and the temperature profile can be obtained across the sample for any given time.

Figure 5.11 shows the flow chart for this coupled electro-, thermo- and kinetic model. Essentially, the material property (complex permittivity for the DGEBA/DDS) is updated with the current local temperature and extent-of-cure according to the modified Davidson-Cole model with a sufficiently fine timestep as the thermoset curing is proceeding. At the same time, the time derivative of extent-of-cure (dα/dt), which will be used in the energy balance equation, also is updated according to the kinetics model and by the interpolation between curves with different heating temperature. The extent-of-cure distribution also is updated by performing the integration of the dα/dt over the corresponding timestep. Therefore, in this multiphysics model, the node-based FEM for

heat transfer model together with the finite difference scheme, and the edge-based FEM for the electromagnetic model, will be called alternatively during the time-marching process.
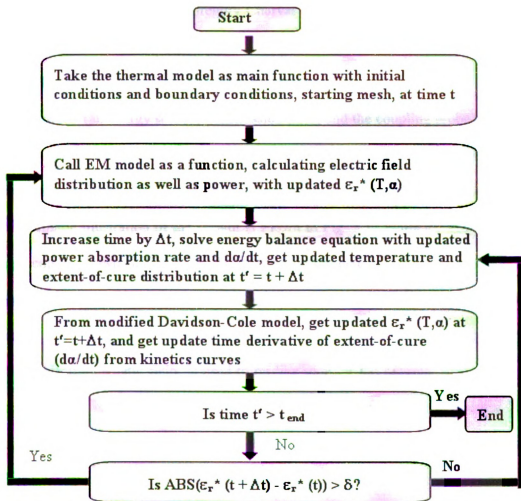

Figure 5.11 Flow chart for the coupled electro-, thermo- and kinetic model.

5.7 Experimental Setup

The microwave diagnostic and processing system at MSU was developed by Dr. Jinder Jow. The details of the system and the single mode perturbation method can be found in his dissertation [54]. A microwave switch between the heating and diagnostic systems was developed by Mr. Gregory Charvat [60]. Here is a brief description of the system.

The microwave diagnostic and processing system consists of a microwave external circuit (an energy source, transmission lines, and the coupling probe), diagnostic elements (i.e. an X-Y oscilloscope, power meters, the E-field diagnostic probe, and a temperature sensor device), and the loaded cavity (i.e. the cavity and the loaded material). The schematic illustration of the system is shown in Fig. 5.12 while the system with the equipments is shown in Fig. 5.13. A single-mode circular cylindrical cavity is used to process epoxy resins at a frequency of 2.45 GHz. A fluoroptic temperature sensing device (Luxtron 750), which does not absorb electromagnetic energy and minimally interferes with the electromagnetic field, is used to on-line monitor the material temperature. The fluoroptic probe is protected by a 3 mm O.D. pyrex capillary tube. A cylindrical Teflon sample holder is also required to contain the liquid samples. The cylindrical geometry of both the cavity and loaded materials is selected in order to facilitate diagnosis, modeling, and theoretical analysis.
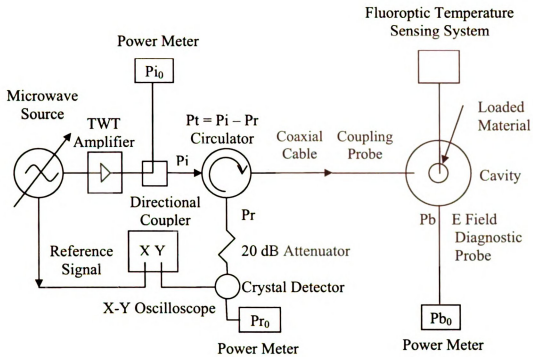
Figure 5.12 Schematic illustration of the microwave processing and diagnostic system.
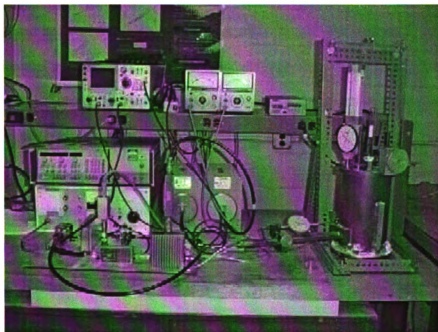

Figure 5.13 Microwave processing and diagnostic system.

As mentioned earlier, in this thesis, the epoxy resin is diglycidyl ether of bisphenol A (DGEBA, DER 332 by Dow Chemical) and the curing agent is 3,3-diaminodiphenyl sulfone (DDS by TCI America). All of the materials were used as received without further purification. In preparing neat DGEBA/DDS epoxy resins, stoichiometric DGEBA and DDS (2.79:1 by weight) were mixed in a glass beaker. The mixtures were well stirred by hand in a 130°C oil bath until the DDS was completely dissolved (in approximately five minutes). Finally, the resins were degassed at 0.02 bar at 100°C for five minutes.

Before the epoxy sample held by the Teflon holder was loaded in the single-mode cavity, the height of the cavity was adjusted such that the TM_{012} mode was excited inside the cavity at 2.45 GHz. The degassed liquid epoxy resins were poured into the Teflon holder. The dimensions of the epoxy resins and the Teflon holder have been described in section 5.5 and in Fig. 5.9, which are the same as here since the numerical model follows the experimental system. Then the Teflon holder with a fluoroptic probe and epoxy resin sample was centrally loaded in the middle of the cavity. Careful and small adjustments need to be done on both the height of the cavity and the position of the Teflon holder such that the sample is located at the place where the electric field is the strongest.

The single frequency microwave curing and diagnostic system was used to heat the liquid samples in the Teflon holder. Usually for the purpose of dielectric property measurement, the procedure is as follows. The fresh DGEBA/DDS samples were heated to react at 145°C for specified reaction time periods, e.g. 1, 5, and 20 minutes, with the exception of those for the 0% cured epoxy resin, which were heated to 100°C. Thereafter,

the single frequency microwave curing system was switched to a low-power swept frequency diagnostic system by changing the switch position. Measurements of temperature and dielectric properties using the swept frequency method were made during free convective cooling of the samples. The cooled samples were analyzed with a Differential Scanning Calorimeter (DSC) to determine the residual heat of reaction per gram and thus the extents of cure.

However, in this study, in order to test the numerical model with the experimental data, only the curing mode (heating mode) was used. The input power was fixed at 5 Watts and the temperature was recorded as it increased. The temperature/time profile generated from the numerical model is compared with the experimental data in the next section.

5.8 Numerical Results vs. Measured Data

Fig. 5.14 shows the comparison between the calculated and measured temperature as a function of time during thermoset curing process. For the positions of point A, B, and C, please refer to fig. 5.9. The measured temperature was taken at the center of the epoxy sample. In the numerical model, $\Delta t = 5$ seconds was used as the timestep and h = 15 $W/m^2/K$ was used as the free convective heat transfer coefficient, which was used in the convective boundary condition. It can be seen that the calculated temperature profile is in good agreement with the measured data.

Figs. 5.15, 5.16, and 5.17 show the calculated extent-of-cure, dielectric constant, and dielectric loss factor as a function of time for the three points during microwave heating. From Fig. 5.16 and Fig. 5.17, it can be seen that both the dielectric constant and

the dielectric loss factor increase as the temperature increases at the beginning, before the curing starts at 125°C. Once the temperature reaches 125°C, the curing process will begin with chemical reactions. As the extent-of-cure increases, both the dielectric constant and the dielectric loss factor decrease. As shown in the expression (5.2), the power absorption rate is related with the dielectric loss factor. As the dielectric loss factor becomes smaller and smaller, the microwave power energy absorbed by the epoxy sample becomes less and less. From Fig. 5.2, it can be seen that the chemical reaction heat reaches maximum at the extent-of-cure around 20% — 30%, and becomes smaller and smaller after that. Fig. 5.14 shows that the temperature reaches the maximum at 250°C and then starts to cool down. However, the extent-of-cure still increases since the temperature is still above 125°C. The final extent-of-cure of the epoxy resins stops at about 80% and the curing process reaches the end.

Fig. 5.18 shows the parametric study on the heat transfer coefficient h with three different values of 5, 15, and 25 (W/m^2/K), and it is clear that the value of h plays a very important role on the accuracy of the numerical model.

Since the epoxy thermoset curing process is exothermic, which means that heat energy is released during the chemical reactions, the term $\rho\dfrac{\partial\alpha}{\partial t}(-\Delta H_r)$ in the energy balance equation (5.9) must be used to account for this. In order to see how significant the chemical reaction heat is, the simulation was run without the term $\rho\dfrac{\partial\alpha}{\partial t}(-\Delta H_r)$ in (5.9), and the result is shown in Fig. 5.19. Apparently, the chemical reaction heat can not be neglected for an accurate model of the process.

78

In this numerical model, the complex permittivity of the DGEBA/DDS was updated as a function of both local temperature and extent-of-cure during heating process. Another two cases were also performed to see how important it is to include these variations. In case 1, the complex permittivity is kept constant ($\varepsilon_r^* = 4 - j0.2$), which is the initial value at the room temperature before the heating process begins. In case 2, the complex permittivity as the function of the local temperature, but not the function of the extent-of-cure, is used. This means the curve with 0% extent-of-cure in the modified Davidson-Cole model is used. All three cases are shown in Fig. 5.20 with the measured data. It is clear that updating the complex permittivity as a function of both temperature and extent-of-cure gives most accurate results.

The temperature distributions at the horizontal cross-section layers containing points A, B, and C respectively are specifically recorded in the numerical model for each timestep during the calculation. As the examples to illustrate the temperature variations in both spatial and temporal domains, the snap-shots of the temperature distribution at the cross section of point B are listed in Figs. 21-26 for the heating time of 100, 300, 400, 500, 700, and 1000 seconds.
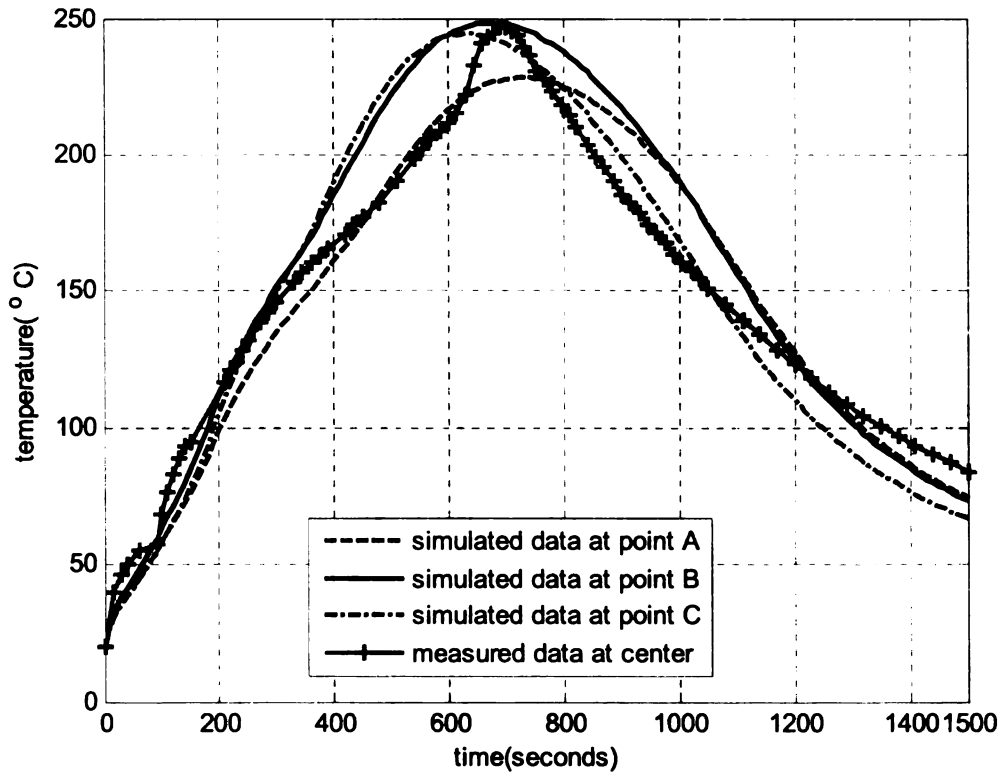
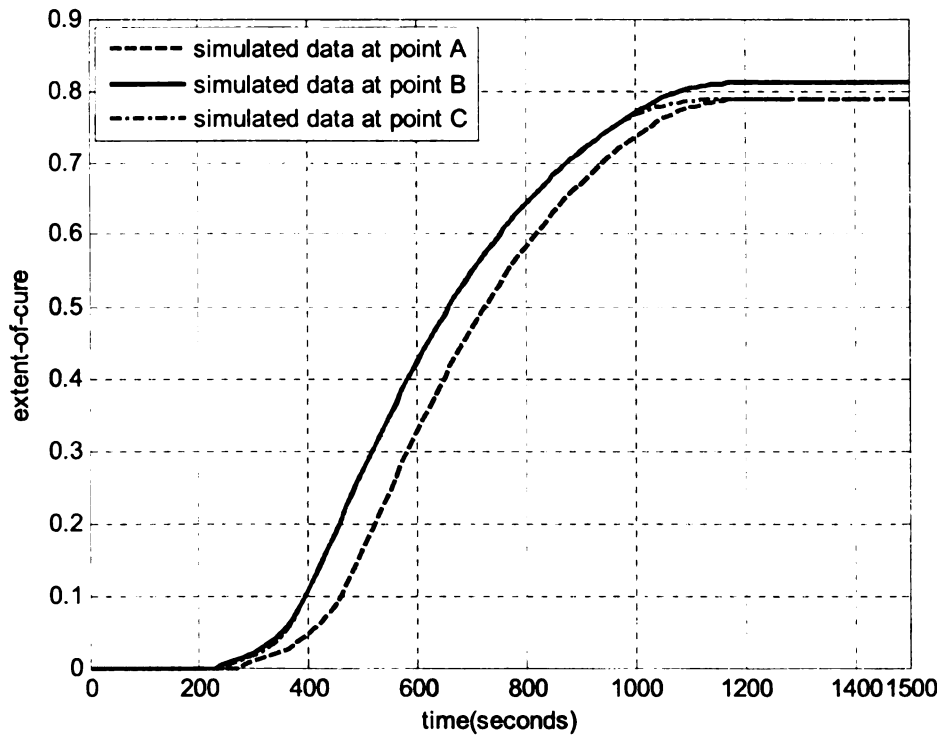Figure 5.14 Calculated and measured temperature vs. time for the epoxy sample.

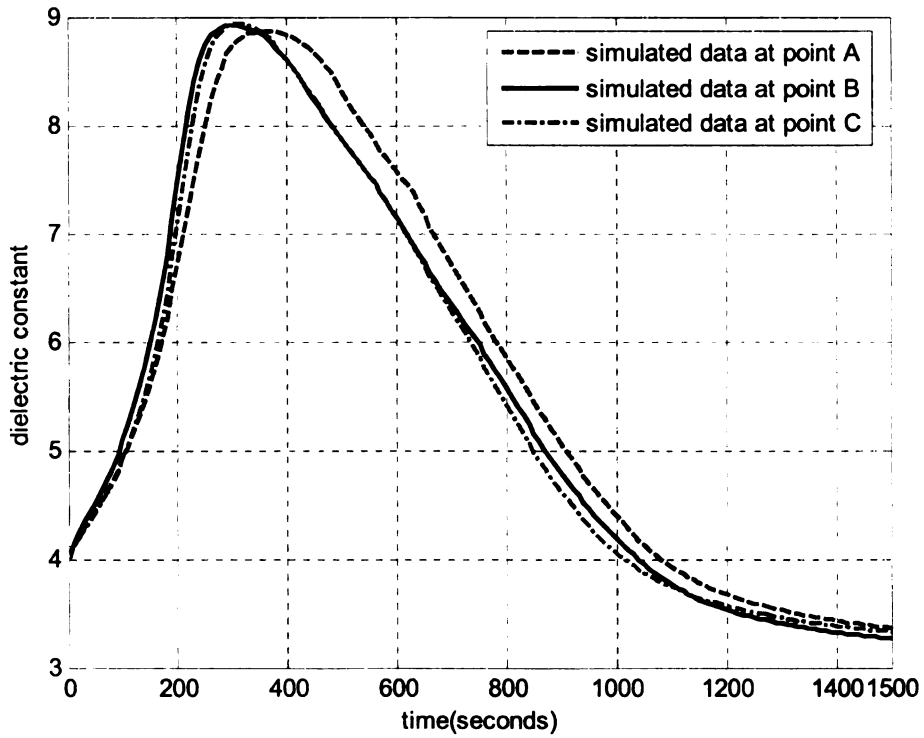Figure 5.15 Calculated extent-of-cure vs. time for the epoxy sample.

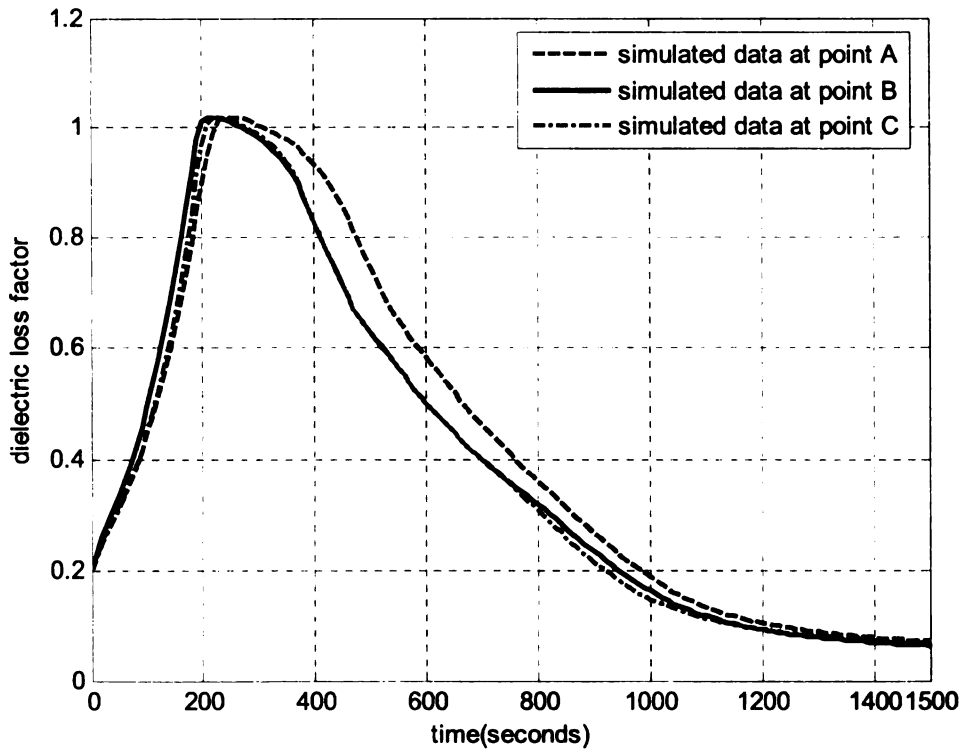Figure 5.16 Calculated dielectric constant vs. time for the epoxy sample.

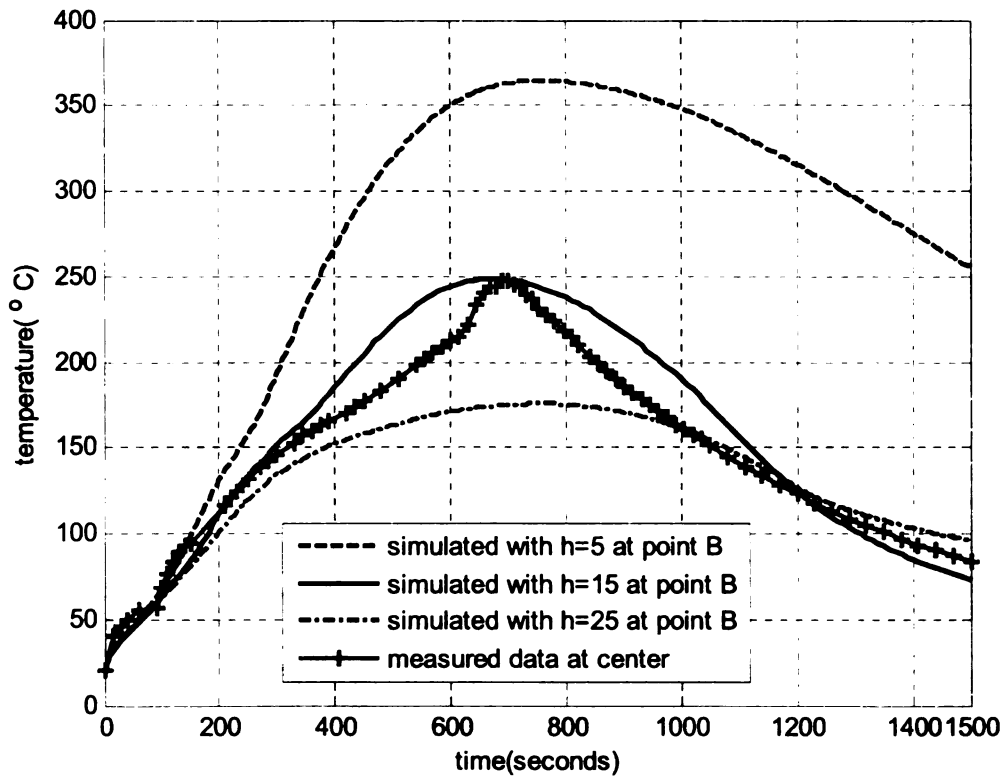Figure 5.17 Calculated dielectric loss factor vs. time for the epoxy sample.

Figure 5.18 Parametric study on the heat transfer coefficient *h* for the epoxy sample.
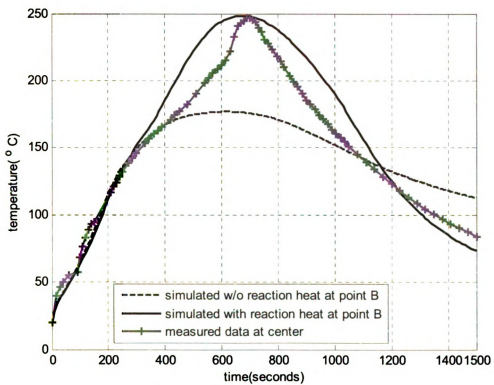
Figure 5.19 Simulation with and without reaction heat for the epoxy sample.
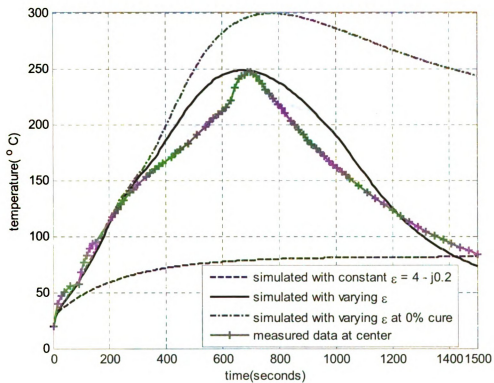
Figure 5.20 Simulation on the variation effects of the complex permittivity for the epoxy

sample.

Figure 5.21 Temperature distribution at cross section of point B at $t = 100$ seconds.

Figure 5.22 Temperature distribution at cross section of point B at $t = 300$ seconds.

Figure 5.23 Temperature distribution at cross section of point B at t = 400 seconds.

Figure 5.24 Temperature distribution at cross section of point B at t = 500 seconds.
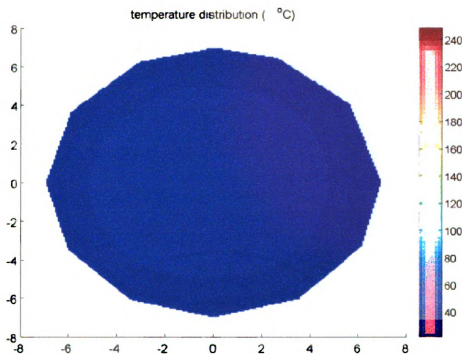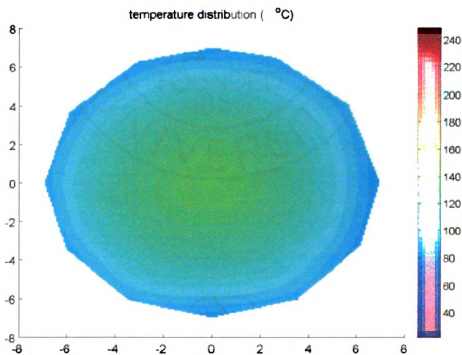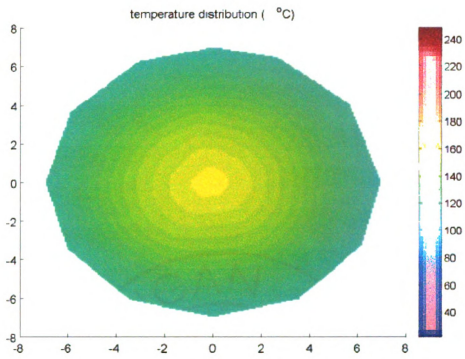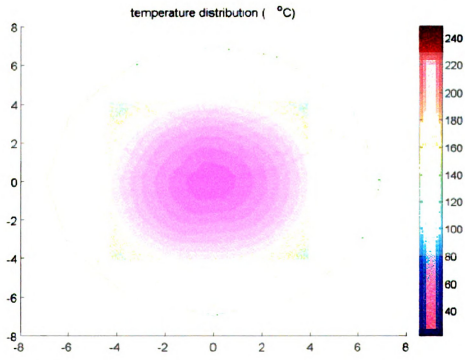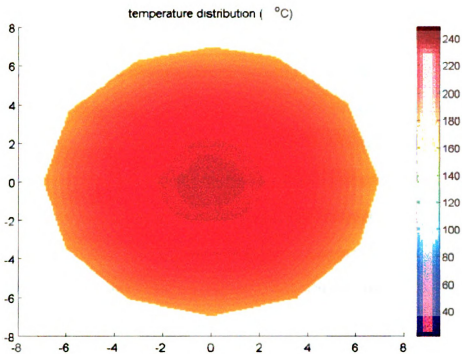
Figure 5.25 Temperature distribution at cross section of point B at t = 700 seconds.
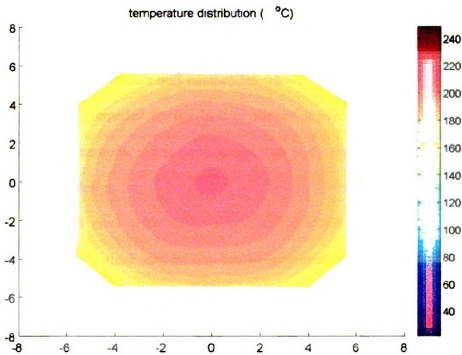

Figure 5.26 Temperature distribution at cross section of point B at t = 1000 seconds.

CHAPTER 6 ADAPTABLE MULTIMODE APPLICATOR MODELING

In this chapter, the electromagnetic modeling of a novel adaptable multi-feed multimode cylindrical cavity applicator is presented, where the spatial distribution of the electric field can be specified *a priori* to accomplish a desired processing task. The electric field intensity inside the cavity can be tailored by varying the power delivered to each port, and mode-switching can be realized without mechanically adjusting the cavity dimensions. An orthogonal feeding mechanism is developed to reduce the cross coupling between the ports. Numerical simulations are performed for the cavity applicator to verify the theoretical analysis.

6.1 Introduction

As mentioned earlier, microwave has been investigated as an attractive and efficient alternative energy source compared to inefficient pressurized ovens for material processing, including polymers and composites. However, industrial use of microwave processing has been impeded by the lack of proper applicator design, modeling, and control/monitoring methods. Most existing applicators are for specific applications only and the applicator design has to be performed over and over again for new processes, mostly by trial and error without the assistance of a model. The development of adaptable applicators, which can be configured to accomplish a variety of processing tasks, is therefore very important.

Commonly used applicators for materials processing can be classified into three basic types: waveguide, multimode and single-mode applicators. A waveguide applicator is a hollow conducting pipe with either a rectangular or a circular cross-section. The

wave inside a waveguide applicator is fundamentally different from that inside multimode and single-mode applicator. The former is a traveling wave and the latter is a standing wave. Energy from the microwave generator travels through the waveguide and is partially absorbed by the material being processed. The remainder of the energy is directed to a terminating load. Traveling wave applicators are primarily used for continuous processing of high-loss materials; low-loss materials require an excessively long waveguide or a long processing period to absorb the necessary energy.

The most popular applicator type is the overmoded or multimode cavity where the electric field distribution is given by the sum of all the modes excited at a particular frequency. The frequent use of multimode cavity applicators is a result of their low cost, simplicity of construction, and adaptability to many different heating loads. This kind of applicator is very versatile in that it can accept a wide range of material loads of different dielectric losses, size and shape [61]. However, that may limit product quality, particularly with regard to the uniformity of temperature distribution in processed materials. Difficulties for multimode cavity analysis of electric field distributions result essentially from coexistence of many resonant modes. By rotating the sample and/or using metal stirrers, it is possible to improve the E-field uniformity and, thus, the heating uniformity inside the multimode applicator [62]. A mode-stirrer is a fan within a multimode cavity designed to change the resonance of multiple modes within a 4 MHz band near 2.45 GHz. As the mode-stirrer rotates, the resonant conditions of the cavity change, focusing the energy into different field patterns. The rotation of the fan cycles the cavity through the different resonant modes with a pattern that accepts whatever random heating occurs across the sample. This may improve the heating uniformity to a certain

degree, but makes it more difficult to predict the electric field distribution and is not suitable for precision material processing.

The single-mode resonant applicator is designed to support only one resonant mode, therefore resulting in highly localized heating. These applicators can efficiently provide high field strength at mode-specific locations within the cavity since single frequency systems can be tuned for maximum throughput. Although single-mode applicators have a high efficiency relative to multimode and traveling wave applicators, sometimes it is very difficult for them to provide desired uniform heating across a large sample. To obtain uniform heating under these conditions, a technique called mode-switching was developed, in which several modes with complementary heating patterns are alternatively excited [63].

With a fixed frequency microwave power source, mode-switching can be achieved by mechanically adjusting the length of the cavity. This mechanical process slows the response of the system to temperature changes. With a variable frequency power source, modes can be changed by changing frequency. As a result of the instantaneous variable frequency mode switching, not only the speed of the process but also the controllability of the process is much improved [64]. However, variable frequency sources are inherently less efficient than the single frequency versions; the equipment is also very expensive.

In this research effort, mode-switching can be obtained by varying the power delivered to multiple ports, hence eliminating the need for mechanical applicator adjustments.

In this case, the field intensity can be tailored to achieve high field strength in the regions of the applicator requiring high fields (and hence regions where heating is desirable) and low field intensities in regions where heating is not desired. Multi-port, multi-feed applicators will be studied where the field spatial distribution can be specified *a priori* to accomplish a desired processing task. Single frequency operation is preferred since the over-all system efficiency is generally higher for such "tuned" systems.

Specifically, in our modeling, a cylindrical cavity is excited via two ports to get a TM mode and a TE mode simultaneously. With these separately controllable TM and TE modes, not only is the desired field strength distribution obtained at specific locations inside the cavity, but also the ability to heat along a preferred direction can be achieved; this is particularly useful when anisotropic materials are processed. Taking advantages of TM and TE modes, it is easy for us to get low port-to-port coupling, especially when a lossy load is present. This will be shown later in both theoretical analysis and numerical results.

6.2 Mode-Switching

Typically, inside a cylindrical cavity, TM modes are excited with a coaxial probe while TE modes are excited with sidewall-mounted loops. Although these are useful methods for feeding, they may not lead to sufficient decoupling of the two ports. If the feeds are ideally orthogonal, the mutual coupling between the ports is zero (i.e., $S_{21} = 0 = S_{12}$). This is a desirable condition since a non-zero transmission term indicates that power from one port will exit the cavity through the other port doing no significant heating of the polymer. Our cavity design has two feed ports. The feed mechanism

chosen, to minimize mode cross-coupling, are an axial slot (to excite a TE mode) and an azimuthal slot (to excite a TM mode). These slots are electrically very narrow to avoid mode cross-coupling.

By observing the mode diagrams in Fig. 3.1 and Fig. 3.2, which show the resonant frequency as a function of cavity length for TM and TE modes in an empty cavity with radius $a = 10.75$ cm, it is seen that when the cavity height is adjusted, we can have different combinations of TM and TE modes resonant at 2.45 GHz, and thus get different electric field distribution inside the cavity. When the radius $a = 10.75$ cm and the height $h = 7.34$ cm, we can get the combination of TM_{020} and TE_{211}, which is shown in Fig. 6.1(a); while $a = 10.75$ cm and $h = 9.50$ cm, the combination of TM_{020} and TE_{311} is shown in Fig. 6.1(b). For both cases, we have an axisymmetric electric field pattern (TM_{020}) at the center as well as some distributed spots (TE_{211} or TE_{311}) around it. TM mode has the electric field orientation parallel to the central axis of the cylinder, which is best suited for heating rods and cylinders located along the axis of the cylinder; TE mode has the electric field polarization to the bottom plate of the applicator, which is best suited for heating flat panels or disks.

For each combination of TM and TE mode with fixed cavity height, by varying the power delivered to each port, mode-switching can be obtained at a single frequency without mechanically adjustment of the cavity dimensions. This transition can be shown in fig. 6.2 for the combination of TM_{020} and TE_{211} case. To investigate the electric field distribution for simultaneous mode excitation, a parameter α is introduced. A pure TE mode excitation has $\alpha = 0$ while a pure TM mode excitation is given by $\alpha = 1$. The cavity model was verified for these two cases using the appropriate slot excitation methods. The

numerical simulations using COMSOL's FEMLAB code [35] were performed for different α, which means different relative power delivered to each port. Fig. 6.2 illustrates the field distribution for each α, where (c) is the same as that in fig. 6.1(a) but with different scale. It was determined that $\alpha = 0.55$ yielded the most uniform electric field for curing purpose in the center plane of the applicator. A uniform field is desirable since that will allow the curing of the largest diameter part.
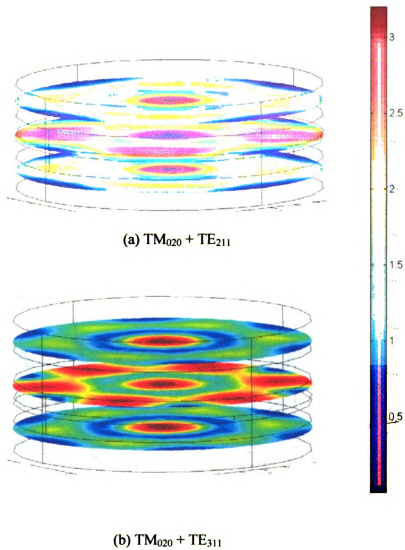
(a) $TM_{020} + TE_{211}$

(b) $TM_{020} + TE_{311}$

Figure 6.1 Electric field distribution for different combination of TM and TE modes.

(a) α = 0

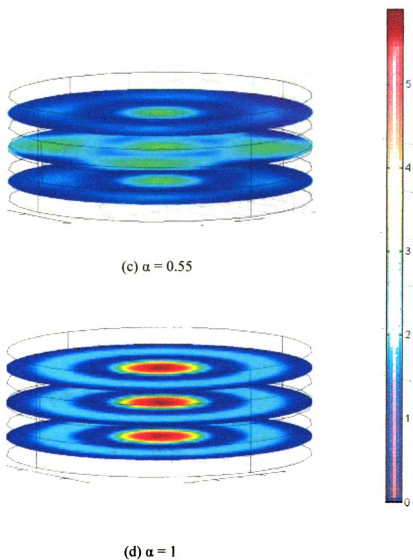(b) α = 0.25

(c) α = 0.55

(d) α = 1
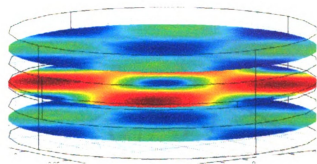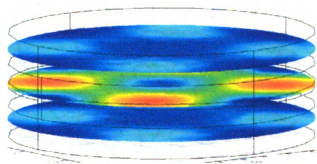
Figure 6.2 Parametric study on the weighting factor α for the combination of the two

modes.

6.3 Port-to-Port Coupling Analysis

As mentioned earlier, the mutual coupling between the two ports is a very important factor that influences the performance of the applicator. To get better performance, lowest possible coupling is needed in order to avoid energy leakage through the ports. In a homogeneous, source-free cylindrical cavity with perfectly conducting walls, the electromagnetic fields inside the cavity can be derived from Maxwell's equations and the boundary conditions [17]. For TM$_{020}$ mode, the fields are given by

$$E_\rho = E_\phi = 0$$

$$E_z = \frac{k^2}{j\omega\varepsilon}J_0\left(\frac{5.52\rho}{a}\right) = -j\omega\mu J_0\left(\frac{5.52\rho}{a}\right) \tag{6.3}$$

$$H_\rho = H_z = 0$$

$$H_\phi = -\frac{\partial \psi_{020}^{TM}}{\partial \rho} = \frac{5.52}{a}J_1\left(\frac{5.52\rho}{a}\right)$$

For TE$_{211}$ mode, the fields are given by

$$E_\rho = -\frac{1}{\rho}\frac{\partial \psi_{211}}{\partial \phi} = \frac{2}{\rho}J_2(\frac{3.054}{a}\rho)\sin(2\phi)\sin(\frac{\pi z}{h})$$

$$E_\phi = \frac{\partial \psi_{211}}{\partial \rho} = \cos(2\phi)\sin(\frac{\pi z}{h})\left[J_1(\frac{3.054}{a}\rho) - \frac{2a}{3.054\rho}J_2(\frac{3.054}{a}\rho)\right]$$

$$E_z = 0 \tag{6.4}$$

$$H_\rho = \frac{1}{j\omega\mu}\frac{\partial^2 \psi_{211}}{\partial \rho \partial z} = \frac{\pi/h}{j\omega\mu}\cos(2\phi)\cos(\frac{\pi z}{h})\left[J_1(\frac{3.054}{a}\rho) - \frac{2a}{3.054\rho}J_2(\frac{3.054}{a}\rho)\right]$$

$$H_\phi = \frac{1}{j\omega\mu}\frac{1}{\rho}\frac{\partial^2 \psi_{211}}{\partial \phi \partial z} = -\frac{2\pi/h}{j\omega\mu\rho}\sin(2\phi)\cos(\frac{\pi z}{h})J_2(\frac{3.054}{a}\rho)$$

$$H_z = \frac{1}{j\omega\mu}\left(\frac{\partial^2 \psi_{211}}{\partial z^2} + k^2 \psi_{211}\right) = \frac{1}{j\omega\mu}\left(\omega^2 \mu\varepsilon - \left(\frac{\pi}{h}\right)^2\right)J_2\left(\frac{3.054}{h}\rho\right)\cos(2\phi)\sin\left(\frac{\pi z}{h}\right)$$

Considering the field generated by azimuthal slot for TM_{020} mode, E_ρ and E_ϕ are zero, and E_z is very difficult to be coupled out through the axial slot; similarly, for the field generated by axial slot for TE_{211} mode, E_z is zero and it is very difficult for E_ρ and E_ϕ to be coupled out through the azimuthal slot. So it is seen that with these two specific modes, a very low port-to-port coupling can theoretically be obtained, which is essential for achieving improved efficiency.

In practice, the microwave power is delivered into the cylindrical cavity by rectangular waveguides (for this work, WR-284) via iris-coupling (shown in Fig. 6.3 as the meshed geometry in FEMLAB). The dominant mode inside the waveguide is TE_{10} mode. The dimensions of the irises need to be fine-tuned such that the S_{11}, S_{21}, S_{22}, and S_{12} are minimized. Under these conditions, the maximum power is delivered to the load for processing purpose. Fig. 6.4 and Fig. 6.5 show the simulated S-parameters for this empty two-port cavity, where the TE-port is denoted as port 1 and TM-port is shown as port 2. The resonant frequency shifted down a little bit from 2.45 GHz due to the existence of the irises. After the lossy epoxy samples are loaded inside the cavity, the S_{21} and S_{12} are expected to be even smaller. Since the complex permittivity of epoxy resins varies as a function of temperature and extent-of-cure during microwave heating, the S_{11} and S_{22} are expected to vary significantly due to the loaded epoxy sample. In practice, in order to adjust the reflection coefficients at the two ports, a brass plunger can be

100

introduced lying very close to each coupling iris [65], such that the S_{11} and S_{22} can be retuned in real-time.

Currently, the iris-coupled two-port cavity is being built and the feed network that includes the coax-to-waveguide transition is also being implemented. Experiments will be carried out to verify the model and the control strategies will be developed for microwave thermoset curing of epoxy resins.
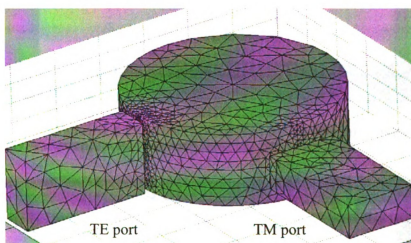

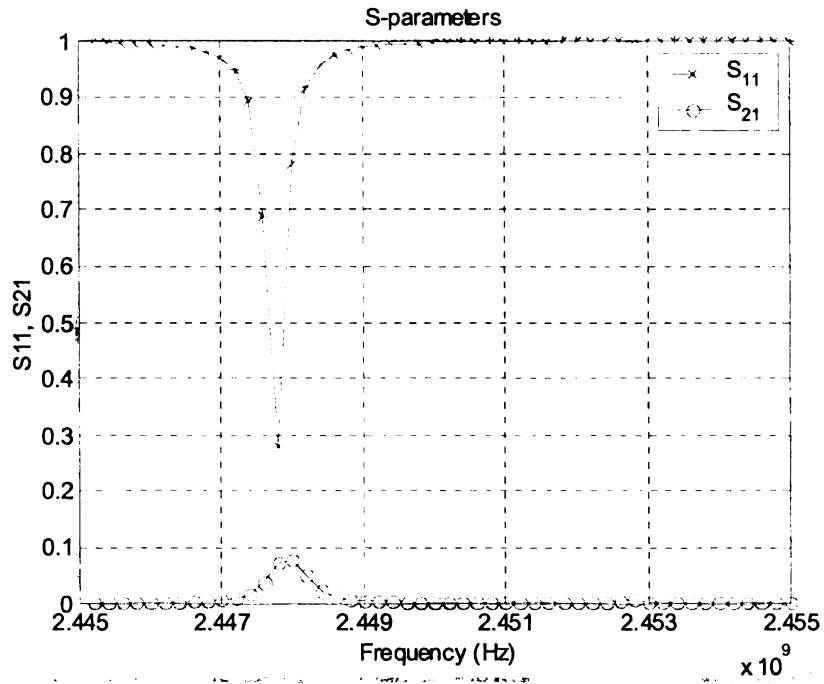Figure 6.3 The two-port cavity fed with waveguides via irises.

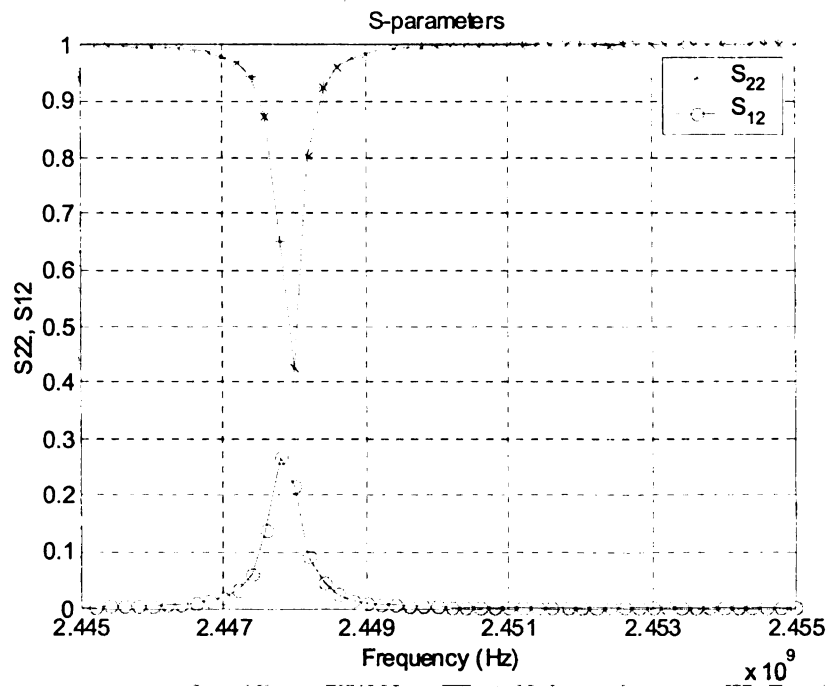Figure 6.4 TE mode (S_{11} and S_{21}) for the two-port cavity.

Figure 6.5 TM mode (S_{22} and S_{12}) for the two-port cavity.

CHAPTER 7 CONCLUSIONS

In this study, a self-consistent 3D marching-in-time multiphysics model has been developed, which includes electromagnetic field distribution, microwave power absorption, heat transfer, and polymer curing kinetics. The temperature- and cure-dependent permittivity and curing kinetics for DGEBA/DDS based on experimental data were explicitly included in the model. Edge-based FEM was implemented for electromagnetic model to ensure the tangential continuity of electric field and divergence-free condition for source free region, while node-based FEM was used in thermal model to solve for the temperature distribution. The numerical results can be used to determine the time-dependent temperature distribution and curing profile across the polymer sample, as well as the electromagnetic field distribution within the cavity applicator. With the help of this numerical model, robust control strategies can be developed for the polymer curing process. The numerical results have been compared with the measured data and a good agreement was achieved.

The electromagnetic modeling of a novel adaptable multi-feed multimode cylindrical cavity applicator was presented, where the spatial distribution of the electric field can be specified *a priori* to accomplish a desired processing task. It has been shown that the electric field intensity inside the cavity can be tailored by just varying the power delivered to each port, and the mode-switching can be realized without mechanically adjusting the cavity dimensions. An orthogonal feeding mechanism was developed to reduce the cross coupling between the ports. Numerical simulations were performed for the cavity applicator to verify the theoretical analysis.

CHAPTER 8 RECOMMENDATIONS FOR FUTURE WORK

The recommendations for the future work include the following:

1. The dielectric property measurements need to be done at higher temperature, up to 250°C for DGEBA/DDS epoxy resins with different extents of cure at 2.45 GHz, in order to get accurate values of the complex permittivity. This may be difficult since the extent of cure keeps changing at high temperature. A better model than Davidson-Cole model should be investigated that has the ability to account for the high temperature and different extent of cure.

2. The automatic microwave processing and diagnostic system should be developed such that the dielectric constant and dielectric loss factor can be measured and recorded real time as the heating process is proceeding.

3. In this study, the input power delivered to the cavity was kept constant and recorded the temperature as it increased during the thermoset curing process. The main purpose of this is to test the numerical model. In practice, the heat temperature is usually kept constant during the curing process while the level of the input power is being adjusted. So in order to make the code useful for practical applications, especially on developing feedback control strategies, the modification should be done in the model accordingly.

4. After the two-port multimode cavity is built, experiments are expected to be carried out to verify the model and the control strategies should be developed for microwave thermoset curing of epoxy resins. A non-

invasive online monitoring technique should be developed as well, to

provide feedback to the control system.

APPENDIX EXPRESSIONS FOR INTEGRAL TERM WITH DOT PRODUCT

In section 4.2.2, to evaluate the integral $F_{ij}^e = \iiint_{V^e} \mathbf{W}_i^e \cdot \mathbf{W}_j^e dV$, first the dot

product is obtained as

$$\mathbf{W}_i^e \cdot \mathbf{W}_j^e = \frac{l_i^e l_j^e}{(6V^e)^2}\left[L_{i_1}^e L_{j_1}^e f_{i_2 j_2} - L_{i_1}^e L_{j_2}^e f_{i_2 j_1} - L_{i_2}^e L_{j_1}^e f_{i_1 j_2} + L_{i_2}^e L_{j_2}^e f_{i_1 j_1} \right]$$

where $j_{ij} = b_i^e b_j^e + c_i^e c_j^e + d_i^e d_j^e$. Substituting this into the integral and utilizing the

general integration formula given in (4.11), each entry in the elemental matrix can be

obtained analytically [22]. For completeness, the expressions for these entries are listed

below

$$F_{11}^e = \frac{(l_1^e)^2}{360V^e}(f_{22} - f_{12} + f_{11})$$

$$F_{12}^e = \frac{l_1^e l_2^e}{720V^e}(2f_{23} - f_{21} - f_{13} + f_{11})$$

$$F_{13}^e = \frac{l_1^e l_3^e}{720V^e}(2f_{24} - f_{21} - f_{14} + f_{11})$$

$$F_{14}^e = \frac{l_1^e l_4^e}{720V^e}(f_{23} - f_{22} - 2f_{13} + f_{12})$$

$$F_{15}^e = \frac{l_1^e l_5^e}{720V^e}(f_{22} - f_{24} - f_{12} + 2f_{14})$$

$$F_{16}^e = \frac{l_1^e l_6^e}{720V^e}(f_{24} - f_{23} - f_{14} + f_{13})$$

$$F_{22}^e = \frac{(l_2^e)^2}{360V^e}(f_{33} - f_{13} + f_{11})$$

$$F_{23}^e = \frac{l_2^e l_3^e}{720V^e}(2f_{34} - f_{13} - f_{14} + f_{11})$$

$$F_{24}^e = \frac{l_2^e l_4^e}{720V^e}(f_{33} - f_{23} - f_{13} + 2f_{12})$$

$$F_{25}^e = \frac{l_2^e l_5^e}{720V^e}(f_{23} - f_{34} - f_{12} + f_{14})$$

$$F_{26}^e = \frac{l_2^e l_6^e}{720V^e}(f_{13} - f_{33} - 2f_{14} + f_{34})$$

$$F_{33}^e = \frac{(l_3^e)^2}{360V^e}(f_{44} - f_{14} + f_{11})$$

$$F_{34}^e = \frac{l_3^e l_4^e}{720V^e}(f_{34} - f_{24} - f_{13} + f_{12})$$

$$F_{35}^e = \frac{l_3^e l_5^e}{720V^e}(f_{24} - f_{44} - 2f_{12} + f_{14})$$

$$F_{36}^e = \frac{l_3^e l_6^e}{720V^e}(f_{44} - f_{34} - f_{14} + 2f_{13})$$

$$F_{44}^e = \frac{(l_4^e)^2}{360V^e}(f_{33} - f_{23} + f_{22})$$

$$F_{45}^e = \frac{l_4^e l_5^e}{720V^e}(f_{23} - 2f_{34} - f_{22} + f_{24})$$

$$F_{46}^e = \frac{l_4^e l_6^e}{720V^e}(f_{34} - f_{33} - 2f_{24} + f_{23})$$

$$F_{55}^e = \frac{(l_5^e)^2}{360V^e}(f_{22} - f_{24} + f_{44})$$

$$F_{56}^e = \frac{l_5^e l_6^e}{720V^e}(f_{24} - 2f_{23} - f_{44} + f_{34})$$

$$F_{66}^e = \frac{(l_6^e)^2}{360V^e}(f_{44} - f_{34} + f_{33}).$$

REFERENCES

1. J. Wei, M. C. Hawley, and J. D. Delong, "Comparison of Microwave and Thermal Cure of Epoxy Resins," *Polymer Engineering and Science*, vol. 33, no. 17, pp. 1132-1140, 1993.

2. D. A. Lewis, J. C. Hedrick, T. C. Ward, and J. E. McGrath, "The Accelerated Curing of Epoxy Resins Using Microwave Radiation," *Polymer Preprints*, vol. 28, no. 2, pp. 330-331, 1987.

3. R. Agrawal and L.T. Drzal, "Effects of Microwave Processing on Fiber-Matrix Adhesion in Composites," *Journal of Adhesion*, vol. 29, pp. 63-79, 1989.

4. J. Wei, J. Jow, J. D. DeLong, and M. C. Hawley, "Microwave Processing of Crossply Continuous Graphite Fiber/Epoxy Composites," *SAMPE Journal*, vol. 27, no. 1, pp. 33-39, 1991.

5. M. LeGrand and V. Bellenger, "The Cure Optimisation of Carbon/Epoxy Prepregs," *Composite Science and Technology*, vol. 58, no. 5, pp. 639-644, 1998.

6. M. A. Acitelly, R. B. Prime, and E. Sacher, "Kinetics of Epoxy Cure: (1) The System Bisphenol-A Diglycidyl Ether/*m*-phenylene Diamine," *Polymer*, vol. 12, no. 5, pp. 335-343, 1971.

7. G. L. Hagnauer, P. J. Pearce, B. R. Laliberte, and M. E. Roylance, in *Thermorheology of Thermosetting Polymers*, pp. 25-47, C. A. May, ed., Washington, D.C., 1983.

8. A. Dutta and M. E. Ryan, "Effect of fillers on Kinetics of Epoxy Cure," *Journal of Applied Polymer Science*, vol. 24, no. 3, pp. 635-649, 1979.

9. J. Mijovic, "Cure Kinetics of Neat Versus Reinforced Epoxies," *Journal of Applied Polymer Science*, vol. 31, no. 5, pp. 1177-1187, 1986.

10. A. Moroni, J. Mijovic, E. M. Pearce, and C. C. Foun, "Cure Kinetics of Epoxy Resins and Aromatic Diamines," *Journal of Applied Polymer Science*, vol. 32, no. 2, pp. 3761-3773, 1986.

11. J. Wei, M. C. Hawley and M. T. Demeuse, "Kinetics Modeling and Time-Temperature-Transformation Diagram of Microwave and Thermal Cure of Epoxy Resins," *Polymer Engineering and Science*, vol. 35, no. 6, pp. 461-470, 1995.

12. Z. Fathi, D. A. Tucker, W. A. Lewis, and J. B. Wei, "Industrial Applications of Variable Frequency Microwave Energy in Materials Processing," *Microwave Processing of Materials V, Materials Research Society Symposium Proceedings*, vol. 430, pp. 21-28, 1996.

13. V. Adegbite, "Automation and Control of the Microwave Processing of Composite Materials," Ph.D. Dissertation, Michigan State University, 1995.

14. Y. Qiu, V. Adegbite, and M.C. Hawley, "Intelligent Composite Processing Using Variable Frequency Method: Preliminary Heating Results," 27th *International SAMPE Technical Conference Proceedings*, pp.173-183, 1995.

15. Y. Qiu and M. C. Hawley, "Automated Variable Frequency Microwave Processing of Graphite/Epoxy Composite in a Single Mode Cavity," *Proceedings of the 13th Annual Technical Conference, American Society for Composites*, 1998.

16. Y. Qiu, "Variable Frequency Microwave Processing and Microwave Process Control for Polymer Composites," Ph.D. Dissertation, Michigan State University, 2000.

17. R. F. Harrington, *Time-Harmonic Electromagnetic Fields*, McGraw-Hill, New York, 1987.

18. C. C. Ku, and R. Liepins, *Electrical Properties of Polymers: Chemical Principles*, Hanser, Munich, 1987.

19. C. Saltiel and A. K. Datta, "Heat and Mass Transfer in Microwave Processing," *Advances in Heat Transfer*, vol. 33, pp. 1-94, 1999.

20. L. Zong, S. Zhou, R. Sun, L. C. Kempel, and M. C. Hawley, "Dielectric Analysis of a Crosslinking Epoxy Resin at a High Microwave Frequency," *Journal of Polymer Science Part B: Polymer Physics*, vol. 42, no. 15, pp. 2871-2877, 2004.

21. J. L. Volakis, A. Chatterjee, and L. C. Kempel, *Finite Element Method for Electromagnetics: Antennas, Microwave Circuits, and Scattering Application*, New York: IEEE Press, 1998.

22. Jianming Jin, *The Finite Element Method in Electromagnetics*, second edition, Wiley-Interscience, New York, 2002.

23. P. P. Silvester and R. L. Ferrari, *Finite Elements for Electrical Engineers* (2nd edition). Cambridge: Cambridge University Press, 1990.

24. Z. J. Csendes and P. Silvester, "Numerical Solution of Dielectric Loaded Waveguides: I — Finite Element Analysis," *IEEE Trans. Microwave Theory Tech.*, vol. 18, no. 12, pp. 1124-1131, 1970.

25. X. Yuan, D. R. Lynch, and K. Paulsen, "Importance of Normal Field Continuity in Inhomogeneous Scattering Calculations," *IEEE Trans. Microwave Theory Tech.*, vol. 39, no. 4, pp. 638-642, 1991.

26. H. Whitney, *Geometric Integration Theory*. Princeton University Press, NJ, 1957.

27. A. Bossavit and J. C. Verite, "A Mixed FEM-BIEM Method to Solve 3D Eddy Current Problems," IEEE Trans. Magnetics, vol. 18, no. 2, pp. 431-435, 1982.

28. J. C. Nedelec, "Mixed Finite Elements in R^3," Numer. Math., vol. 35, pp. 315-341, 1980.

29. M. Hano, "Finite Element Analysis of Dielectric-Loaded Waveguides," *IEEE Trans. Microwave Theory Tech.*, vol. 32, no. 10, pp. 1275-1279, 1984.

30. A. Bossavit, "Whitney Forms: A Class of Finite Elements for Three-Dimensional Computations in Electromagnetism," *IEE Proceedings*, vol. 135, pt. A, no. 8, pp. 493-500, 1988.

31. A. E. Bogle, "Electromagnetic Material Characterization Using a Partially Filled Rectangular Waveguide," Master Thesis, Michigan State University, 2004.

32. A. Melloni, M. Politi, and G. G. Gentili, "Mode-Matching Analysis of TE_{011}-Mode Waveguide Bandpass Filters," *IEEE Trans. Microwave Theory Tech.*, vol. 43, no. 9, pp. 2109-2116, 1995.

33. G. L. Matthaei, L. Young, and E. M. T. Jones, *Microwave Filters Impedance-Matching Networks and Coupling Structures*. New York: McGraw-Hill, 1964.

34. F. Shnurer, "Design of aperture-coupled filters," *IRE Trans. Microwave Theory Tech.*, pp. 238-243, Oct. 1957.

35. COMSOL, Inc., *FEMLAB User's Manual*, version 3.0a, 2004.

36. P. Ratanadecho, K. Aoki, and M. Akahori, "Experimental Validation of a Combined Electromagnetic and Thermal Model for a Microwave Drying of Capillary Porous Materials inside a Rectangular Wave Guide," *Journal of Microwave Power & Electromagnetic Energy,* vol. 37, no. 1, pp. 15-40, 2002.

37. L. Pichon and O. Meyer, "Coupled Thermal-Electromagnetic Simulation of a Microwave Curing Cell," *IEEE Transactions on Magnetics*, vol. 38, no. 2, pp. 977-980, 2002.

38. B. Wappling-Raaholt, et al., "A Combined Electromagnetic and Heat Transfer Model for Heating of Foods in Microwave Combination Ovens," *Journal of Microwave Power & Electromagnetic Energy,* vol. 37, no. 2, pp. 97-111, 2002.

39. H. Zhang and A. Datta, "Coupled Electromagnetic and Thermal Modeling of Microwave Oven Heating of Foods," *Journal of Microwave Power & Electromagnetic Energy,* vol. 35, no. 2, pp. 71-85, 2000.

40. Z. Huang, M. Iskander, J. Tucker, and H. Kimrey, "FDTD Modeling of Realistic Microwave Sintering Experiments," Materials Research Society Symposium Proceedings, vol. 347, pp. 331-345, 1994.

41. V. Soriano, C. Devece, and E. De los Reyes, "A Finite Element and Finite Difference Formulation for Microwave Heating Laminar Material," *Journal of Microwave Power & Electromagnetic Energy*, vol. 33, no. 2, pp. 67-76, 1998.

42. L. Pham and K. Pope, "3D Finite Element Model of RF Heating: Novel Non-Ablative Cutaneous Therapy," *Proceedings of SPIE*, vol. 4949, pp. 22-31, 2003.

43. J. Haala and W. Wiesbeck, "Modeling Microwave and Hybrid Heating Processes Including Heat Radiation Effects," *IEEE Trans. Microwave Theory Tech.*, vol. 50, no. 5, pp. 1346-1354, 2002.

44. T. V. C. T. Chan, J. Tang and F. Younce, "3-Dimensional Numerical Modeling of an Industrial Radio Frequency Heating System Using Finite Elements," *Journal of Microwave Power & Electromagnetic Energy*, vol. 39, no. 2, pp. 87-105, 2004.

45. Q. Tang, N. Tummala, S. K. S. Gupta, and L. Schwiebert, "Communication Scheduling to Minimize Thermal Effects of Implanted Biosensor Networks in Homogeneous Tissue," *IEEE Trans. Biomedical Engineering*, vol. 52, no. 7, pp. 1285-1294, 2005.

46. K. G. Ayappa, H. T. Davis, G. Crapiste, E. A. Davis, and J. Gordon, "Microwave Heating: an Evaluation of Power Formulations," *Chemical Engineering Science*, vol. 46, no. 4, pp. 1005-1016, 1991.

47. S. Zhou, "Interactions in Microwave Adhesive Bonding of Polymers and Composites," Ph.D. Dissertation, Michigan State University, 2002.

48. L. Zong, "Microwave Processing of Epoxy Resins and Synthesis of Carbon Nanotubes by Microwave Plasma Chemical Vapor Deposition," Ph.D. Dissertation, Michigan State University, 2005.

49. H. Lee and K. Neville, *Epoxy Resins: Their Applications and Technology*, McGraw-Hill, New York, 1957.

50. J. O. Simpson and S. A. Bidstrup, "Rheological and Dielectric Changes During Isothermal Epoxy-Amine Cure," *Journal of Polymer Science Part B: Polymer Physics*, vol. 33, no. 1, pp. 55-62, 1995.

51. D. W. Davidson and R. H. Cole, "Dielectric Relaxation in Glycerol, Propylene Glycol, and n-Propanol," Journal of Chemical Physics, vol. 19, pp. 1484-1490, 1951.

52. W. Kauzmann, "Dielectric Relaxation as a Chemical Rate Process," Reviews of Modern Physics, vol. 14, no. 1, pp. 12-44, 1942.

53. G. Gallone, S. Capaccioli, G. Levita, P.A. Rolla, S. Corezzi, "Dielectric Analysis of the linear Polymerization of an Epoxy Resin," Polymer International, vol. 50, pp. 545-551, 2001.

54. J. Jow, "Microwave Processing and Dielectric Diagnosis of Polymers and Composites Using a Single-Mode Resonant Cavity Technique," Ph.D. Dissertation, Michigan State University, 1988.

55. Skyblue Systems, *SKY/Mesh2 user's manual*, version 2.33, 1999.

56. J. Meese, L. Kempel, and S. Schneider, "Subdividing Distorted Prisms into Tetrahedra," *19th Annual Review of Progress in Applied Computational Electromagnetics*, Monterey, CA, March 2003.

57. D. R. Kincaid and T. C. Oppe, "ITPACK on Supercomputers," *Numerical Methods: Lecture Notes in Mathematics*, vol. 1005, pp. 151-161, 1982.

58. C. Lanczos, "Solution of Systems of Linear Equations by Minimized Iterations," *J. Res. Natl. Bur. Stand.*, vol. 49, pp. 33-53, 1952.

59. J. Heinrich and D. Pepper, *Intermediate Finite Element Method: Fluid Flow and Heat Transfer*. PA: Taylor & Francis, 1999.

60. L. Zong, G. L. Charvat, L. C. Kempel, and M. C. Hawley. "Automated method for characterizing temperature dependent dielectric materials," *26th AMTA Meeting & Symp.*, Stone Mountain, GA, Oct., 2004.

61. J. E. Gerling, "Microwave Oven Power: a Technical Review," *Journal of Microwave Power and Electromagnetic Energy*, vol. 22, no. 4, pp. 199-207, 1987.

62. A. C. Metaxas and R. J. Meredith, *Industrial Microwave Heating*, pp. 137-138, IEE Power Engineering Series, Peter Peregrinus Ltd., London, 1983.

63. L. A. Fellows and M. C. Hawley, "Microwave Heating of Composites with Complex Geometries in Cylindrical Single-Mode Resonant Microwave Cavities," *Proceedings of the 29th Microwave Power Symposium*, pp. 91-94, Chicago, IL, July 1994.

64. Y. Qiu and M. C. Hawley, "Computer Controlled Variable Frequency Microwave Processing of Complex-Shaped Graphite/Epoxy Composite," *Proceedings of the 14th American Society for Composites Annual Technical Conference*, pp. 52-61, Dayton, OH, September 1999.

65. L. Chen, C. K. Ong, and B. T. G. Tan, "A Resonant Cavity for High-Accuracy Measurement of Microwave Dielectric Properties," *Measurement Science and Technology*, vol. 7, no. 9, pp. 1255-1259, September 1996.